國立臺灣大學理學院應用物理研究所
碩士論文
Graduate Institute of Applied Physics
College of Science
National Taiwan University
Master Thesis

在 Belle II 實驗中用 ECL 資訊辨別 K_L^0 介子
The study of K_L^0 Identification with ECL Information at Belle II experiment

蘇鉦皓
Jheng-Hao Su

指導教授：王名儒教授
Advisor: Min-Zu Wang, Professor

中華民國 112 年 6 月
June, 2023

Acknowledgements

I would like to thank my advisor, Professor Min-Zu Wang, who pointed out a direction and helped me in the research. I would not be able to complete this thesis without his assistance.

Thank Doctor Jing-Ge Shiu for giving me some advices about my research topic. In addition, thank Doctor Giuseppe Finocchiaro, Doctor Alessandro Di Cicco, and Yu-Tan Chen for providing some detail information for this study.

I would also like to thank Chuan-Yu Chang, Kai-Ning Chu, Kun-Xian Huang, Jie-Cheng Lin, Yuan-Ru Lin, Jen-Yu Tau, Han-Sheng Wang, Wen-Yi Chen, and Wei-Che Lin for giving me some supports in the laboratory.

摘要

我們可以透過從 ECL 束或 KLM 束所重建的 K_L^0 粒子列表來研究 K_L^0 介子。粒子識別 (PID) 可以幫助我們將 K_L^0 從其它粒子，如光子、中子、反中子，和其他電中性粒子區分開來。本論文使用 Belle II 實驗中 ECL 的資訊並描述識別 K_L^0 粒子之建立、方法、表現及比較。

在這篇論文中，我們使用快速提升決策樹 (FastBDT) 以獲得訓練過後的多變量分析方法。此方法可以將訊號 (K_L^0) 以及背景 (K_L^0 以外的所有電中性粒子)。我們呈現重建 $B^0 \to J/\psi K_L^0$ 衰變的初步結果，其中 J/ψ 會衰變成 $\mu^+\mu^-$，而 K_L^0 介子是從 ECL 裡的中性強子束重建而來。在 Belle II 實驗中使用蒙地卡羅方法單純產生訊號，我們可以從 100 萬個事件裡得到 25% 的效率。使用蒙地卡羅方法生成各種粒子時，我們可以從 $100 fb^{-1}$ 的光度獲得 681 ± 71 個訊號事件。此外，我們也使用 Belle II 實驗在 SuperKEKB 的非對稱能量 e^+e^- 對撞機所收集到光度 $189.049 fb^{-1}$ 的數據。在 $J/\psi \to \mu^+\mu^-$ 的情況下，我們總共量測到 1031 ± 95 個訊號事件。我們也比較了上述的結果與從 KLM 裡的 K_L^0 介子重建 $B^0 \to J/\psi K_L^0$ 衰變的結果。透過在訊號生成與真實數據中比較 ECL 和 KLM 在全範圍以及訊號範圍的結果，我們發現 ECL 和 KLM 並沒有太大的重複性。因此本論文提供了 K_L^0 識別的另一個方法。

關鍵字:Belle II，K_L^0 介子，識別，ECL，FastBDT

Abstract

We can study K_L^0 through K_L^0 particle list reconstructed from ECL cluster or KLM cluster. Particle identification (PID) can help separate K_L^0 from other particles, like γ, neutron, anti-neutron and other neutral particles. This thesis shows the establishment, method, performance and the comparison of K_L^0 particle identification by using only ECL information in Belle II experiment.

In this thesis, we use Fast Boosted Decision Tree (FastBDT) to get a trained multivariate analysis (MVA) method which can separate signal (K_L^0) and background (neutral particles excluding K_L^0). We present the results on the reconstruction of the $B^0 \to J/\psi K_L^0$ decay, where $J/\psi \to \mu^+\mu^-$. K_L^0 mesons are reconstructed from the hadronic neutral clusters in the Electromagnetic Calorimeter (ECL). Using signal Monte Carlo (MC) with one millon events in Belle II, we have about 25% efficiency. In generic MC corresponding to a luminosity of $100 fb^{-1}$, we get 681 ± 71 candidates. Moreover, we use the Belle II experiment dataset corresponding to a luminosity of $189.049 fb^{-1}$ collected in the asymmetric energy e^+e^- collider at SuperKEKB. We measure 1031 ± 95 candidates with $J/\psi \to \mu^+\mu^-$ in total. We also compare the results above with the reconstruction of the $B^0 \to J/\psi K_L^0$ decay, while K_L^0 mesons are reconstructed from the hadronic neutral clusters in K_L^0 and muons (KLM) subdetector. By the comparison of the result in ECL and KLM in whole region and signal region with signal MC and Data, we no-

tice that the overlap of ECL and KLM is not large. This provides another way for K_L^0 identification.

Keywords: Belle II, K_L^0, identification, ECL, FastBDT

Contents

List of Figures

List of Tables

Chapter 1 Introduction

In 2012, the groups at the Large Hadron Collider (LHC) discover of the Higgs boson with mass approximately 125 GeV, providing informations on particle mass generation and electroweak symmetry breaking (EWSB). It allows people to claim all the particles participate in the Standard Model (SM) has been found. [1, 2] However, there are also a lot of physics that can not be explained by the standard model, such as dark matter, dark energy, mass of neutrino, etc. Therefore, there are still many experiments going on and trying to make new discoveries. Belle is one of these experiments.

The Belle experiment was started in 1999 and ended at 2010. This experiment was executed by the Belle Collaboration at the High Energy Accelerator Research Organisation (KEK) in Japan. In June 2010, the upgrade of Belle, Belle II experiment was approved and it started operation in 2018. At SuperKEKB, which is the upgraded KEKB accelerator, Belle II is proposed to offer a larger integrated luminosity. These experiments produce the $\Upsilon(4S)$, which decays to B meson pairs, and this resonance has the mass equal to the energy of colliding electrons (e^-) with positrons (e^+) at the center-of-mass (CoM) frame. This B mesons production gives the oppotunity of the observation of large Charge-Parity (CP) violation.

In the Standard Model, CP-violation comes from electroweak interactions. At the hadronic part, it is described by Cabibbo-Kobayashi-Maskawa (CKM) quark-mixing matrix with an irreducible phase and three angles. The measurements of CP asymmetries in neutral B decays to CP eigenstates $B^0 \rightarrow J/\psi K^0$ give the value of $\sin(2\phi)$ [3]. The angle ϕ comes from the unitarity triangle of the CKM matrix and it is given by $\arg(-V_{cd}V_{cb}^*/V_{td}V_{tb}^*)$ for neutral B decay. In the B meson system, people have constructed

CP violation from a variety of B meson decays. $B^0 \to J/\psi K^0$ is one of those decays, moreover, it has theoretical interpretation and clean clear experimental signatures. This process links the angle ϕ to the measurement of the time-dependent CP asymmetry. Since K_L^0 is a different mixed eigenstate of K^0 and $\bar{K}^0$ from K_S^0, the measurements of $\sin(2\phi)$ in $B^0 \to J/\psi K_L^0$ and $B^0 \to J/\psi K_S^0$ decay are independent. K_L^0 is important to the former decay and the K_S^0 does similar on the latter one. Hence, the identification of these particles is necessary.

In this thesis, we use ECL information to identify K_L^0. In Chapter 2, a brief review of Standard Model and Belle II experiment is provided. In Chapter 3, the method to identify K_L^0 and the performance are discussed. In Chapter 4, we reconstruct the decay of $B^0 \to J/\psi K_L^0$, while $J/\psi \to \mu^+\mu^-$ and K_L^0 mesons are from ECL cluster. We check this among signal MC with one million events, 100 fb^{-1} generic MC (including $B\bar{B}$ and $q\bar{q}$), and 189 fb^{-1} Belle II dataset. In Chapter 5, we reconstruct the above decay which K_L^0 mesons are from KLM cluster among signal MC, generic MC , and Data. Then, comparing the consequences to find out the difference of ECL and KLM. Finally, a summary of this thesis is given.

Chapter 2 The Standard Model and Belle II

In this chapter, a brief review of Standard Model particles and Belle II experiment would be presented. In particular, the review of Standard Model gives an overview of the fundamental particles and the relationships between these particles and the forces. Besides, the CP-violation in the quark sector of SM is introduced, which brings the CKM matrix and the meson CP-violation. Furthermore, several subdetectors in Belle II experiment are discussed, including CDC, SVD, ECL, KLM, etc.

2.1 Standard Model

Standard Model decribes three types of forces as gauge interaction. Strong interaction lies in $SU(3)_C$ gauge group, which is able to explain the interaction between quarks and gluons, providing the mechanism of binding quarks into hadrons. [4] For the other two forces, weak interaction is in $SU(2)_L$ gauge group, and electromagnetic interaction is described by $U(1)_{EM}$ gauge group. However, these two forces is depicted together by $SU(2)_L \times U(1)_Y$ electroweak gauge theory.

People mark the quarks and gluons by using three kinds of colors, red, green, and blue. While a quark can be in one of three conditions, and its color can be changed by emitting or absorbing a gluon. The gluons have eight different types, with color and anti-color together. In addition, gluons couple to gluons as well, this coupling makes the coupling strength large at low energy. Therefore, we can only see hadrons like mesons or baryons, but not the individual quark.

$SU(2)_L$ shows that only left handed fermions have weak interaction. Particles with electric charge take part in electromagnetic force. Furthermore, there is also a kind of scalar boson called Higgs boson in Standard Model, and it is also in $SU(2)_L \times U(1)_Y$ gauge group. However, the Higgs boson breaks $SU(2)_L \times U(1)_Y$ gauge, and gives mass to fermions and the gauge bosons in weak interaction.

All particles in the Standard Model are listed in Tab. 2.1. In this table, the particles q_L , U_R, D_R transform as triplet under $SU(3)_C$ group, each include 3 components. The q_L and l_L represent $SU(2)_L$ left-handed quark and lepton as $SU(2)_L$ doublet. Besides, U_R, D_R, and E_R are right-handed up-type quarks, right-handed down-type quarks and right-handed charged leptons. For fermions, each fermion represents three flavors. G^a_μ represents glouns, which transforms as an octet in $SU(3)_C$, W^b_μ transforms as triplet in $SU(2)_L$, and B_μ transform as singlet in $U(1)_Y$.

Last but not least, H represents $SU(2)_L$ scalar field doublet, and its charge conjugate field of H is defined as

$$\tilde{H} \equiv H^c = i\sigma_2 H^* = \begin{pmatrix} H_0 \\ -H^- \end{pmatrix} \tag{2.1}$$

which transforms in $SU(2)_L$ and has hypercharge $-1/2$.

Gauge Group	$SU(3)_C$	$SU(2)_L$	$U(1)_Y$
$q_L = \begin{pmatrix} U_L \\ D_L \end{pmatrix}$	3	2	1/6
U_R	3	1	2/3
D_R	3	1	-1/3
$l_L = \begin{pmatrix} \nu_L \\ E_L \end{pmatrix}$	1	2	-1/2
E_R	1	1	-1
G^a_μ	8	1	0
W^b_μ	1	3	0
B_μ	1	1	0
$H = \begin{pmatrix} H^+ \\ H^0 \end{pmatrix}$	1	2	1/2

Table 2.1: All the particles in SM. The convention used here is $Q = T^3 + Y$.

2.2 CP-violation

The previous section gives a simple introduction to Standard model. In this section, the violation of the combination of charge symmetry and parity symmetry, which is called CP-violation [5], will be brief introduced.

In the weak interactions of leptons and quarks are the only place where CP violating effects can be accommodated in the Standard Model.

In the neutral kaon system, people had the first experimental observation of CP violation. The kaons $K^0(d\bar{s})$ and $\bar{K}^0(s\bar{d})$ are the lightest mesons having strange quarks, so they can only decay through the weak interaction. K^0 and $\bar{K}^0$ are the eigenstates of the strong interaction and they are referred to their flavor states, not the mass eigenstates. With the mass near 498 MeV, which is relatively light, the neutral kaons only decay to final states with $\pi^+\pi^-$ (pions) or $\mu^+\mu^-/e^+e^-$ (leptons) allowed kinematically. The neutral kaons can also mix between K^0 and $\bar{K}^0$ by the weak interaction with the mechanism shown in Fig. 2.1.

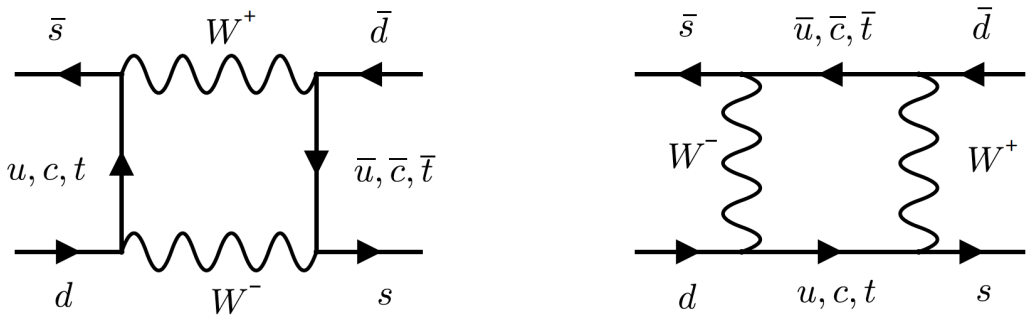

Figure 2.1: The two diagrams of Kaon mixing. [6]

In this figure of kaon mixing, for example, d to $u\,c\,t$, we need the weak interactions of quarks in the Standard Model. They are expressed in terms of the unitary three-generation Cabibbo-Kobayashi-Maskawa (CKM) matrix. The weak eigenstates and the mass eigenstates are related by

$$\begin{pmatrix} d'_L \\ s'_L \\ b'_L \end{pmatrix} = \begin{pmatrix} V_{ud} & V_{us} & V_{ub} \\ V_{cd} & V_{cs} & V_{cb} \\ V_{td} & V_{ts} & V_{tb} \end{pmatrix} \begin{pmatrix} d_L \\ s_L \\ b_L \end{pmatrix}. \tag{2.2}$$

The weak interaction of quarks to the W^+ boson is then

$$-i\frac{g_W}{\sqrt{2}} \begin{pmatrix} \bar{u}_L & \bar{c}_L & \bar{t}_L \end{pmatrix} \gamma^\mu W^+_\mu \begin{pmatrix} V_{ud} & V_{us} & V_{ub} \\ V_{cd} & V_{cs} & V_{cb} \\ V_{td} & V_{ts} & V_{tb} \end{pmatrix} \begin{pmatrix} d_L \\ s_L \\ b_L \end{pmatrix}. \tag{2.3}$$

If the weak interaction had CP symmetry, we would have the two states $|K_1\rangle$ and $|K_2\rangle$ as the CP eigenstates of the neutral kaon system. They are the orthogonal linear combinations of K^0 and $\bar{K}^0$, where

$$|K_1\rangle = \frac{1}{\sqrt{2}}(|K^0\rangle + |\bar{K}^0\rangle) \quad \text{and} \quad |K_2\rangle = \frac{1}{\sqrt{2}}(|K^0\rangle - |\bar{K}^0\rangle) \tag{2.4}$$

The CP eigenstates are

$$\hat{C}\hat{P}\,|K_1\rangle = +\,|K_1\rangle \quad \text{and} \quad \hat{C}\hat{P}\,|K_2\rangle = -\,|K_2\rangle \tag{2.5}$$

If the neutral kaons decays were CP conserving, the hadronic decays of the CP-eigenstates $|K_1\rangle$ and $|K_2\rangle$ would be exactly $K_1 \to \pi\pi$ and $K_2 \to \pi\pi\pi$. We can identified the observed short-lived K^0_S , which decays mostly to two pions, as an approximation to the CP-even state K_1

$$|K^0_S\rangle \approx |K_1\rangle = \frac{1}{\sqrt{2}}(|K^0\rangle + |\bar{K}^0\rangle) \tag{2.6}$$

and the long-lived K_L^0 as an approximation to the CP-odd state K_1

$$|K_L^0\rangle \approx |K_2\rangle = \frac{1}{\sqrt{2}}(|K^0\rangle - |\bar{K}^0\rangle) \tag{2.7}$$

However, we noticed that both K_S^0 and K_L^0 would decay to $\pi\pi$ or $\pi\pi\pi$. With the observation of CP-violation is relatively small in kaon mixing, we can introduce a small complex parameter ϵ, which relates K_S^0 and K_L^0 to the CP eigenstates.

$$|K_S^0\rangle = \frac{1}{\sqrt{1+|\epsilon|^2}}(|K_1\rangle + \epsilon\,|K_2\rangle) \quad \text{and} \quad |K_L^0\rangle = \frac{1}{\sqrt{1+|\epsilon|^2}}(|K_2\rangle + \epsilon\,|K_1\rangle). \tag{2.8}$$

This provides the first evidence of CP-violation.

The CKM matrix is unitary in the Standard Model. This places some constraints on the values of the matrix elements. The constraints are usually written in terms of unitarity triangles. For instance, the unitarity of the CKM matrix shows that

$$V_{ud}V_{ub}^* + V_{cd}V_{cb}^* + V_{td}V_{tb}^* = 0 \tag{2.9}$$

For $V_{td} = |V_{td}|e^{-i\phi_1}$, the angle ϕ_1 corresponds to one of the angles in the unitarity triangle shown in Fig. 2.2. As a result, the measurement of $\sin(2\phi_1)$ constrains the angle between two of the sides of the unitarity triangle.

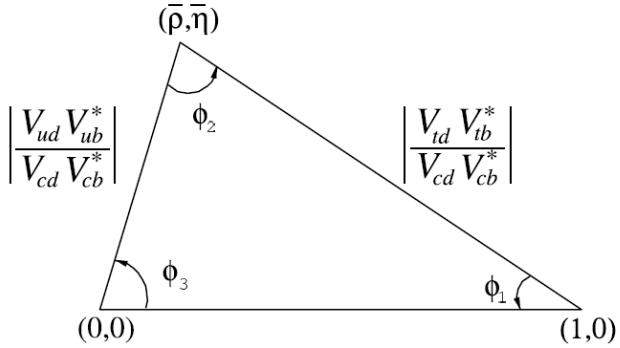

Figure 2.2: The sketch of the unitarity triangle. [7]

The decay rate of of B^0 and $\bar{B}^0$ [8] is given by

$$\Gamma(t) = \frac{e^{-|t|/\tau_{B^0}}}{4\tau_{B^0}}\{1 + q[\mathcal{S}_f \sin(\Delta m_d t) + \mathcal{A}_f \cos(\Delta m_d t)]\} \tag{2.10}$$

τ_{B^0} is the lifetime of B^0, q is 1 for B^0 and -1 for $\bar{B}^0$, Δm_d is the mass difference of two neutral B mass eigenstates, $\mathcal{S}_f$ is $-\sin(2\phi_1)$ for CP-even state and $\mathcal{S}_f$ is $\sin(2\phi_1)$ for CP-odd state, and $\mathcal{A}_f$ is 0 for the $b \to c\bar{c}s$ transition. We can get $\sin(2\phi_1)$ in the interference between $B^0 \to J/\psi K_S^0$ and $B^0 \to \bar{B}^0 \to J/\psi K_S^0$ through the asymmetry,

$$\begin{aligned} A_{CP}^{K_S^0} &= \frac{\Gamma(\bar{B}^0 \to J/\psi K_S^0) - \Gamma(B^0 \to J/\psi K_S^0)}{\Gamma(\bar{B}^0 \to J/\psi K_S^0) + \Gamma(B^0 \to J/\psi K_S^0)} \\ &= \frac{[1 + \sin(\Delta m_d t)\sin(2\phi_1)] - [1 - \sin(\Delta m_d t)\sin(2\phi_1)]}{[1 + \sin(\Delta m_d t)\sin(2\phi_1)] + [1 - \sin(\Delta m_d t)\sin(2\phi_1)]} \\ &= \frac{2\sin(\Delta m_d t)\sin(2\phi_1)}{2} = \sin(\Delta m_d t)\sin(2\phi_1) \end{aligned} \tag{2.11}$$

and $\sin(2\phi_1)$ in the interference between $B^0 \to J/\psi K_L^0$ and $B^0 \to \bar{B}^0 \to J/\psi K_L^0$,

$$\begin{aligned} A_{CP}^{K_L^0} &= \frac{\Gamma(\bar{B}^0 \to J/\psi K_L^0) - \Gamma(B^0 \to J/\psi K_L^0)}{\Gamma(\bar{B}^0 \to J/\psi K_L^0) + \Gamma(B^0 \to J/\psi K_L^0)} \\ &= \frac{[1 - \sin(\Delta m_d t)\sin(2\phi_1)] - [1 + \sin(\Delta m_d t)\sin(2\phi_1)]}{[1 - \sin(\Delta m_d t)\sin(2\phi_1)] + [1 + \sin(\Delta m_d t)\sin(2\phi_1)]} \\ &= \frac{-2\sin(\Delta m_d t)\sin(2\phi_1)}{2} = (-1)\sin(\Delta m_d t)\sin(2\phi_1) \end{aligned} \tag{2.12}$$

We can see the two asymmetries are just different by a negative sign.

For the measurements of $\sin(2\phi_1)$, the $B^0 \to J/\psi K_L^0$ decay is independent of $B^0 \to J/\psi K_S^0$. Moreover, the two decays have different CP eigenvalues. The decays $B^0 \to J/\psi K_L^0$ and $B^0 \to J/\psi K_S^0$ have an identical time-dependent CP asymmetry but with opposite sign. This situation gives us a significant check of the effects on $\sin(2\phi_1)$ measurements.

2.3 SuperKEKB

SuperKEKB [9] is a double-ring collider with e^+e^- having different energy, which is an upgrade of KEKB in order to probe new physics beyond the Standard Model. SuperKEKB has the design with the luminosity, which is higher than the achievement by KEKB. The Belle collaboration obtained a variety of important experimental results about elementary particle physics by using these data and succeeded in proving the Kobayashi-Maskawa theory.

The SuperKEKB collider is made up of a positron ring, which is the low-energy ring (LER), an electron ring, which is the high-energy ring (HER), and an electron-positron injector (LINAC) with a 1.1-GeV positron damping ring (DR). The schematic image is shown in Fig. 2.3.

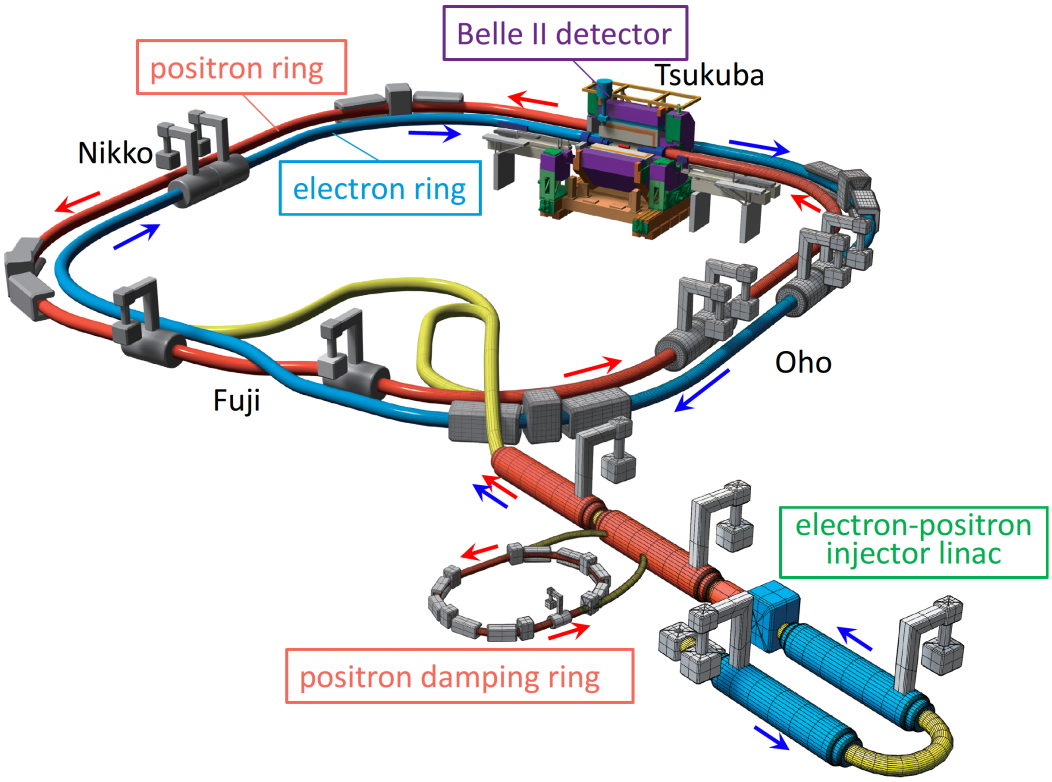

Figure 2.3: The schematic view of SuperKEKB.

The vaule of LER beam energy is 4.0 GeV and the value of HER beam energy is 7.0 GeV in SuperKEKB. LINAC is a linear accelerator and it provides the electron beam and positron beam in two rings of SuperKEKB asymmetric collider for B physics. DR is for

the purpose of reducing positron beam emittance before injecting into the LER.

2.4 Belle II Detector

The Belle II detector [10, 11] consists of several subdetectors, such as PXD, CDC, ECL, KLM, etc. The schematic of the Belle II detector shown in Fig. 2.4. The simple introduction of those subdetectors is provided in the following part.

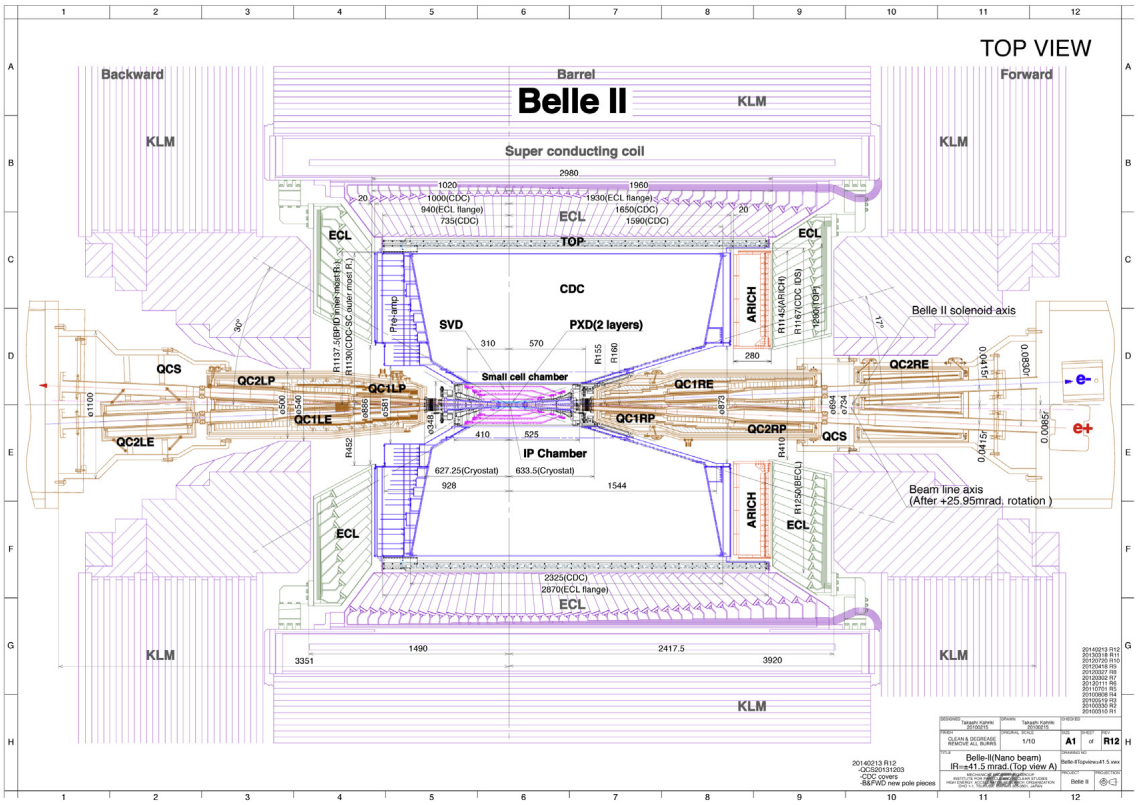

Figure 2.4: The schematic view of Belle II Detector.

2.4.1 Vertex detector (VXD)

For the measurement of mixing-induced CP asymmetry, the main target of the Belle II PXD, SVD, and CDC is to measure the two B decay vertices.

Pixel Detector (PXD)

The detectors near the beam pipe and at the high luminosities designed for SuperKEKB confronts with extremely high hit rates, which caused by low-momentum-transfer QED processes and by beam-related background. It is important to consider such backgrounds carefully when we design the first few layers of the vertex detector. The beampipe radius in the interaction region is almost 10 mm with the nano-beam option selected for the machine of SuperKEKB. This is helpful for the physics about vertex reconstruction. However, since the background increases approximately with the inverse square of the radius, it is also a challenge for the vertex detector. The method to solve this situation is using pixel sensors rather than strips for the innermost layers, which have a larger number of channels. Therefore, the occupancy is much smaller.

The design of pixel detector is based on the technology of DEPleted p-channel Field Effect Transistor (DEPFET), as shown in Fig. 2.5. The DEPFET is a semiconductor detector concept which combines detection and amplification within one device. The DEPFET pixel is equipped with a p-channel metal-oxide-semiconductor field-effect transistor (MOSFET) structure with an internal gate where the electrons can be liberated by traversing charged particles. Besides, the DEPFET pixel consists of a fully depleted silicon substrate .

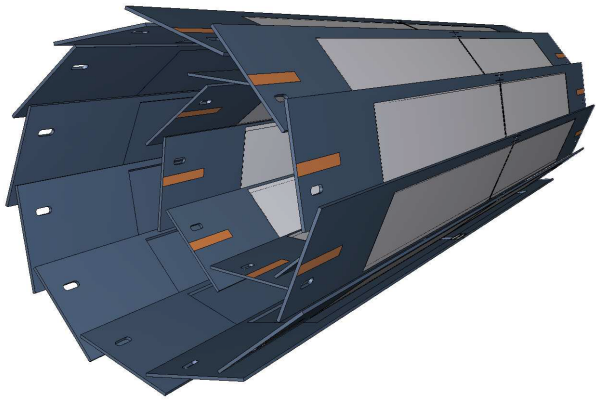

Figure 2.5: The schematic view of Pixel Detector.

Silicon Vertex Detector (SVD)

The SVD is in order to measure the information of vertex in τ-lepton decays and the decay channels involving D-meson.

As shown in Fig. 2.6, the SVD is made from Double-Sided Silicon micro-strip Detectors (DSSDs).

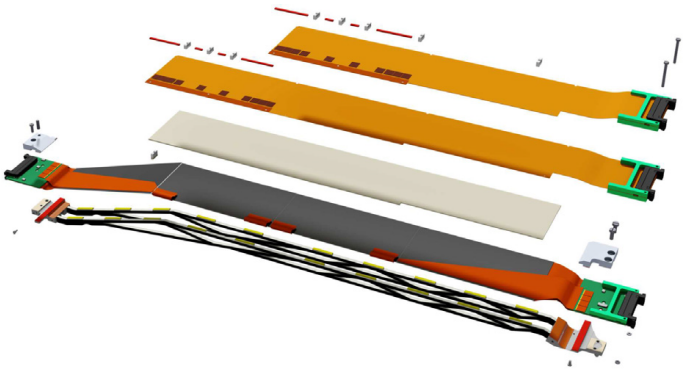

Figure 2.6: The design of SVD.

The double-sided sensors are set up in the way that the large pitch strips at the n-type semiconductor side are perpendicular to the beam direction, and the small pitch strips at p-type semiconductor side are parallel to the beam. These provides the two dimensional coordinate information of the hits. The SVD readout electronics is based on the APV25 chip. All of the requirements on the SVD are satisfied by this APV25 chip. With pipeline readout for dead time-free operation, it has a short pulse shaping time and radiation tolerance of up to 1 MGy.

The SVD covers$17^\circ < \theta < 150^\circ$, which is the full Belle II angular acceptance. The

outer radius is 140 mm and the inner radius is 38 mm. These values are determined by the radii of the CDC and PXD. Moreover, the strategy to determine a vertex is that the SVD gives the data and let the tracks reconstructed in the CDC be extrapolated to the PXD with high efficiency.

It is able to reconstruct low transverse moment tracks, which is down to tens of MeV/c by combining the SVD with the PXD. This will not leave enough hits in the CDC. Particularly, this is important for the efficient reconstruction of the D^* daughters which tag the flavor of the $B^0\bar{B}^0$ meson. Besides, the K_S^0 mesons, decays outside of the PXD volume, can be reconstructed by the SVD. This ability of the SVD is important for the channels like $B \to K_S^0 K_S^0 K_S^0$ or $B \to K^*\gamma$. The only charged tracks are the pions, which are the daughter of K_S^0.

2.4.2 Central Drift Chamber (CDC)

The central drift chamber (CDC) is one of the core euipments of the Belle II spectrometer. It plays some important roles in the Belle II detector. The CDC is a large volume gas drift chamber with small drift cells and the central tracking device. First, it reconstructs charged tracks and measures their momenta precisely. Moreover, by the measurements of energy loss within its gas volume, the CDC gives the information of the particle identification. The CDC can identify the low-momentum tracks, which do not reach the particle identification device, by itself. Furthermore, it provides reliable and efficient trigger signals for charged particles.

The CDC in Belle II has a larger radius than the one in Belle. It consists of a particle identification system in the barrel region. The chamber having smaller drift cells than the one used in Belle is in order to operate with increased background levels at high event rates. As shown in Fig. 2.7, the cell dimensions of the outside layers (10-18 mm) are larger than the innermost 8 layers (6-8 mm) particularly.

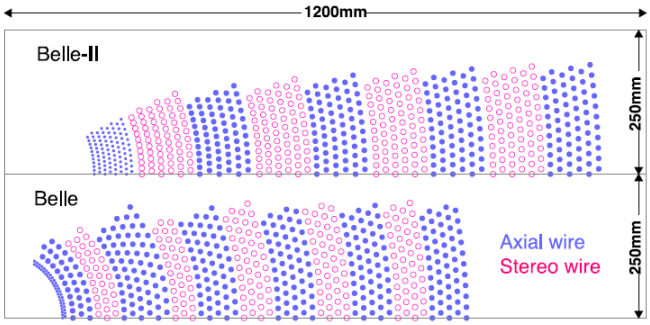

Figure 2.7: The comparison between the wire configurations of the Belle II CDC and the Belle CDC.

2.4.3 Particle identification (PID) system

The subdetector in Particle identification (PID) system are main for identifying kaons and pions since both of them are charged particles with high probability of decay to $\mu^+\nu$. Nevertheless, their mass are different.

Time-of-propagation Detector (TOP)

The time-of-propagation (TOP) counter is used in the barrel region for particle identification. It is a kind of Cherenkov detector. At one end of a 2.6 m long quartz bar, the impact position of Cherenkov photons in the pixel related photo-detectors and the time of arrival provide the two-dimensional information about a Cherenkov ring image. In the total 16 detector modules, each detector module consists of a thick quartz bar with a small expansion volume at the sensor end of the bar. The expansion wedge not only relaxes slightly the precision timing requirements but also introduces some additional pinhole images. Moreover, it can reduce the hit occupancy at the photo-detector

In the situation of a 16-channel Micro-Channel Plate (MCP) Photomultiplier developed specially, the TOP requires photo-sensors with a single photon time resolution of about 100 ps can be achieved. The custom-made pipelined waveform sampling read-out electronics is used for precision timing required in the TOP. In this type of counter, the propagating time of the Cherenkov photons internally reflected inside a quartz radiator can be measured, as shown in Fig. 2.8. We can determine the speed of the particle by

measuring Cherenkov angle θ_c. Since

$$cos(\theta_c) = c/nv \tag{2.13}$$

, where c is the speed of light in vacuum, n is the refractive index in the quartz bar, and v is the speed of the particle. We can get the type of the particle from

$$p = \gamma mv \tag{2.14}$$

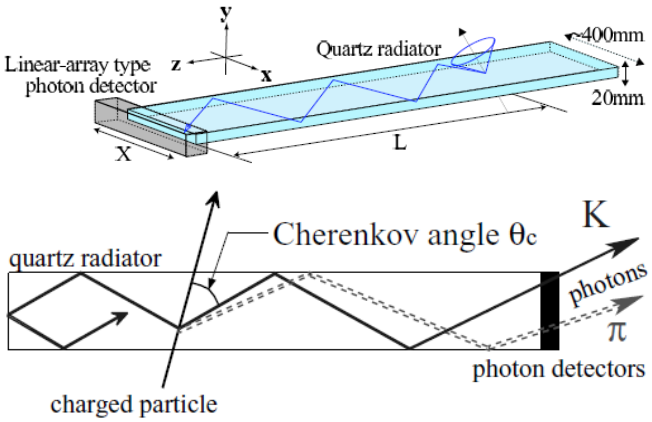

Figure 2.8: The schematic view of TOP counter. (top) The side view of TOP counter and internal reflecting Cherenkov photons. (bottom)

Aerogel Ring-Imaging Cherenkov Detector (ARICH)

As the Cherenkov radiator equipped for identification of the charged particles, the Aerogel Ring-Imaging Cherenkov detector (ARICH) is a proximity focusing Cherenkov ring imaging detector with aerogel in the forward end-cap region. The good separation of pions and kaons up to about 4 GeV/c and a low momentum threshold for pions are the design requirements. It can also separate light charged particles like pions, muons and electrons at momenta below 1 GeV/c.

The ARICH consists of many elements. First, an array of position sensitive photon detectors that is able to detect single photons in a strong magnetic field with high efficiency and good resolution in two dimensions. Second, an expansion volume which can make

Cherenkov photons form rings on the photon detector surface. Third, an aerogel radiator is capable of the charged particles producing Cherenkov photons. Finally, a read-out system for the photon detector. As shown in Fig. 2.9

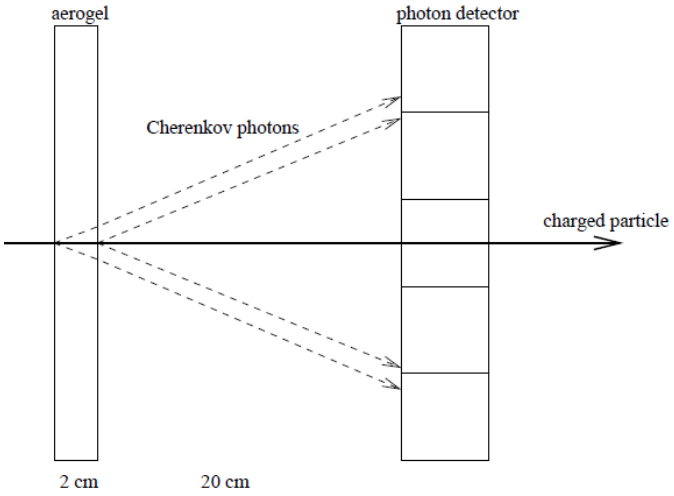

Figure 2.9: The schematic view of ARICH.

2.4.4 Electromagnetic Calorimeter (ECL)

The Electromagnetic Calorimeter (ECL) is a highly-segmented array of thallium-doped cesium iodide CsI(Tl) crystals assembled in a projective geometry shown in Fig. 2.10.

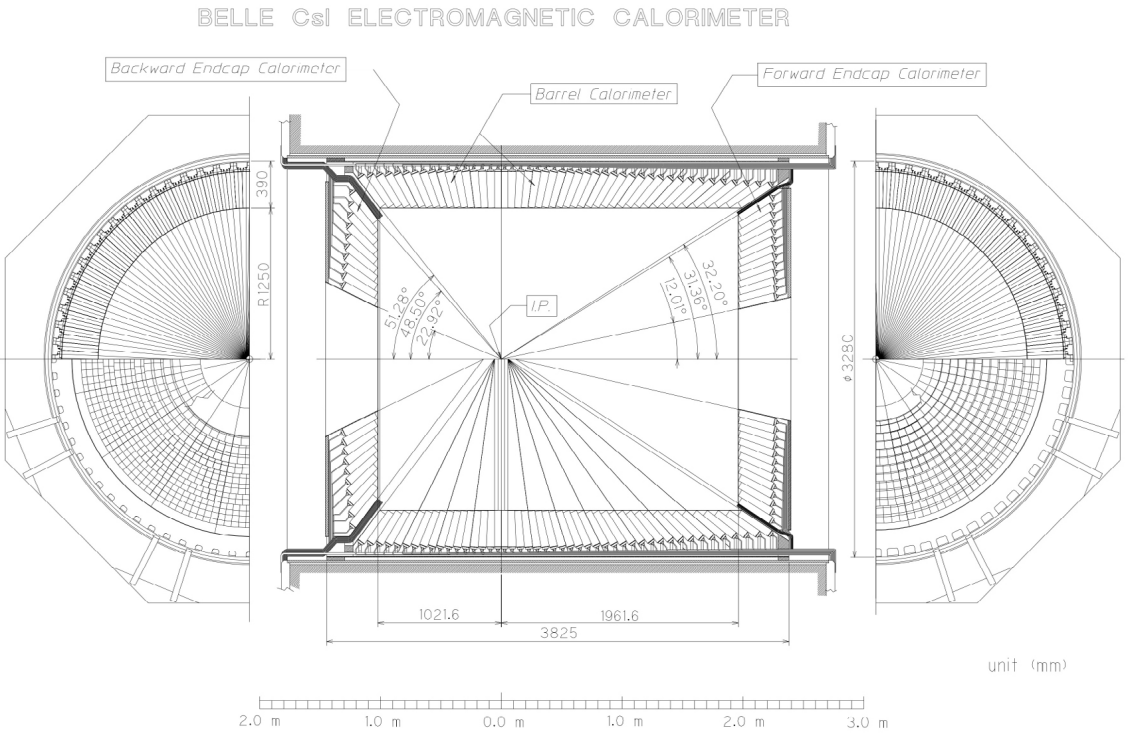

Figure 2.10: The overall configuration of ECL.

Due to its moderate price, good mechanical properties, relatively short radiation length, and high light output, CsI(Tl) is chosen as the scintillation crystal material for the Belle II calorimeter. There are three detector regions, barrel, the forward end-caps, and backward end-caps. All are instrumented with a total of 8,736 crystals. Each crystal is a truncated pyramid of an average size about $6 \times 6cm^2$ in cross section and 30 cm in length. The barrel part contains 6,624 CsI(Tl) crystals of 29 distinct shapes and the end-caps consists of 2,112 CsI crystals of 69 shapes. The geometrical parameters of the ECL are summarized in Tab. 2.2.

	θ coverage	Number of crystals
Barrel	$32.2° - 128.7°$	6624
Forward end-cap	$12.4° - 31.4°$	1152
Backward end-cap	$130.7° - 155.1°$	960

Table 2.2: The geometrical parameters of ECL.

The ECL is used to separate electrons from hadrons, in particular pions. As well as to identify electrons, the ECL detects photons over a wide energy range. Since one third of B-decay products are π^0 or other neutral particles that provide photons in a wide energy range from 0.02 GeV to 4 GeV, a high resolution electromagnetic calorimeter is a important

subdetector of the Belle II detector. The following are several main assignments of ECL. First, detecting the photons with high efficiency and determining the energy and angular coordinates of photons precisely. Second, identifying electrons. In addition, generating the proper signal for trigger and measuring on-line and off-line luminosity. Last but not least, detecting K_L^0 together with the KLM.

2.4.5 K_L^0 - Muon Detector (KLM)

The K_L^0 and muon detector (KLM) is constructed with an alternating sandwich of the active detector elements, which located outside the superconducting solenoid and ECL, plus iron plates layers, as shown in Fig. 2.11.

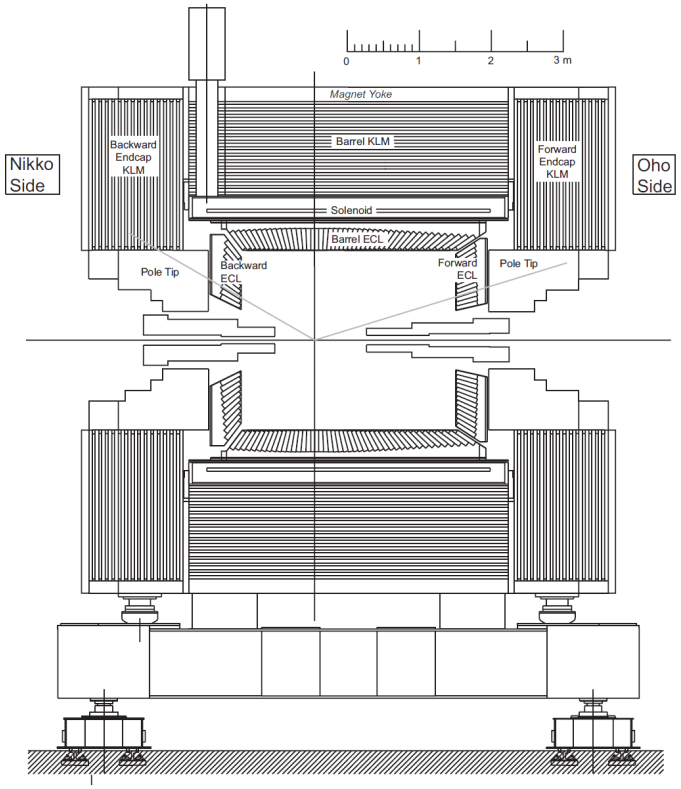

Figure 2.11: The side view of KLM.

The magnetic flux is able to return for the solenoid by the iron plates. Beyond the 0.8 interaction lengths of the calorimeter, the iron plates provide 3.9 or more interaction lengths of the material, so the K_L^0 mesons can shower hadronically. The charged particles are detected by glass electrode Resistive Plate Chambers (RPC) shown in Fig. 2.12. A 1.9 mm thick noryl spacers divided the electrodes, which are two parallel sheets of float glass. The epoxie sticks them in place.

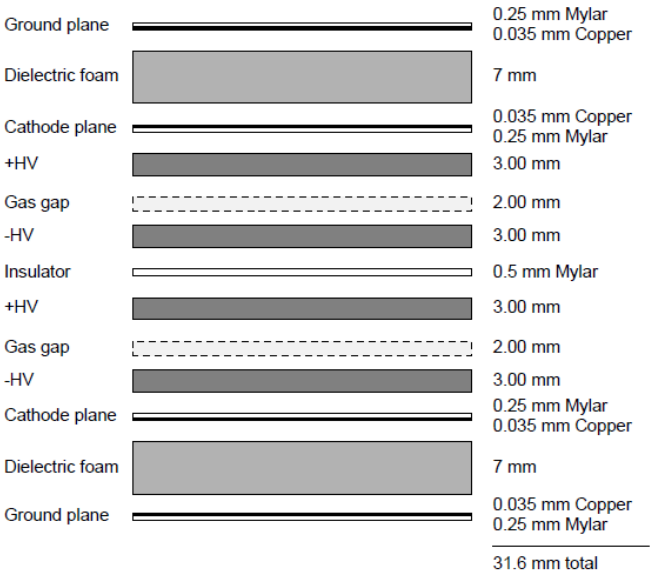

Figure 2.12: The exploded cross-section of RPC.

The reconstruction of a charged track in the CDC is the first step for muon identification. If the track were a pion, that track would be extrapolated outward over the farest place of the CDC hit. If the track crosses one RPC layer, it can be recognized as the acceptance of the KLM. However, the momentum of the track needs to be at least 0.6 GeV/c to cross one RPC layer. A hit of KLM will be associated with the track if it is detected near the crossing of the extrapolated track with a detector layer. Above 1 GeV/c, the efficiency of muon detection is 89% , while the fake rate of the hadron is about 1.3%. The pions neither suffering an inelastic hadronic interaction nor decaying into a softer muon will be the fake muons.

No matter the hits in the KLM is in the same layer or not, the hits within a 5° opening angle of each other are grouped together into a cluster. The charged track veto will be applied after all clusters have been formed. The tracks are extrapolated to their own

entrance into the KLM, then a straight line is drawn between the interaction point and the point of this entrance. The cluster will be discarded if this straight line is in 15° of the line between the interaction point and the cluster centroid. On the other hand, if the cluster is aligned with a reconstructed neutral ECL cluster in 15°, then the ECL cluster will be correlated with the KLM cluster and the direction of cluster in the KLM will be overrided by that in the ECL. The resolution for only KLM candidates is 3°. The one for both KLM and ECL candidates is 1.5°. The efficiency of K_L^0 detection rises almost linearly from 0% to 80% with the momentum of K_L^0 from 0 GeV/c to 3 GeV/c.

2.4.6 Detector Solenoid and Iron Structure

A solenoid located outside of the barrel ECL radially is a superconducting solenoid that gives a 1.5 T magnetic field. It is in a cylindrical volume that the length is 4.4 m and the diameter is 3.4 m. A multi-layer structure, which surrounds the coil, is made by calorimeters and iron plates. Also, it is integrated into a magnetic return circuit.

The iron structure of the Belle II detector serve as an absorber for the KLM and the return path for the magnetic flux of solenoid. In addition, it supports all of the detector components overall. The movable end-cap parts on a base stand and a fixed barrel part comprise the iron structure. The barrel part is built from eight KLM blocks and flux-return plates with 200 mm thick surrounding the outermost layers of the KLM blocks.

2.4.7 Trigger system

The trigger system functions as selecting events of interest. It also rejects the huge background from the Bhabha scattering and the intra-beam scattering. The Belle II trigger allows triggering on all neutral exotic physics signatures like $e^+e^- \to \gamma$ or $e^+e^- \to \gamma A$, where $A \to \gamma\gamma$. In the large QED backgrounds, A represents an Axion-Like-Particle. The Belle II trigger maintains the stability, the good efficiency and the low systematics for $\tau^+\tau^-$ events which provide important input for g - 2 results.

2.4.8 Data Acquisition (DAQ) System

The detector signals upon the Level-1 (L1) trigger decision that given by the trigger system can be read with the data acquisition (DAQ) system. This system transfers the data from the front-end electronics. Through some steps of data processing, the data is finally transfered to the storage system. The Belle2Link, which is the unified data link, the event builder system, the common readout platform called COPPER and the high level trigger (HLT) system are the main components of the data flow. The Belle II DAQ is designed to deal with the trigger rate up to 30 kHz. This value is estimated at full luminosity from the beam-related background and all physics processes.

Chapter 3 MVA Method

Multivariate analysis (MVA) is the statistical study of data where multiple measurements are made on each experimental unit and the relations among these measurements and their structures are important. MVA can calculate the effects of variables, which include physics-based analysis. In this chapter, we identify K_L^0 with MVA method in the Belle II Software. In addition, we provide the performance of this method applied on Monte Carlo (MC).

3.1 Belle II Analysis Software Framework

The Belle II Analysis Software Framework (basf2) [12, 13] is a kind of framework for manipulating Belle II data. The code can be written in both C++ and Python. The modules are algorithms that the users can define and configure it with basf2. The modules are called once per event and put into a path object, which can execute the modules. Users are also able to define the path of modules to be executed in a steering file with a Python application programming interface. Some Python functions have been made for configuring default paths for sections of Belle II processing, like generation of MC events and the reconstruction of track. These software development contributions make the physics analysis easier.

3.2 FastBDT

FastBDT is the default MVA method used in basf2. We will provide the brief introduction about DT, BDT, and FastBDT in the following part. [14, 15]

The classification between signal and background is performed with the FastBDT algorithm. The Decision Tree (DT) performs a classifier that uses a number of consecutive cuts on the input features to hierarchically separate the data, as schematized in Fig. 3.1.

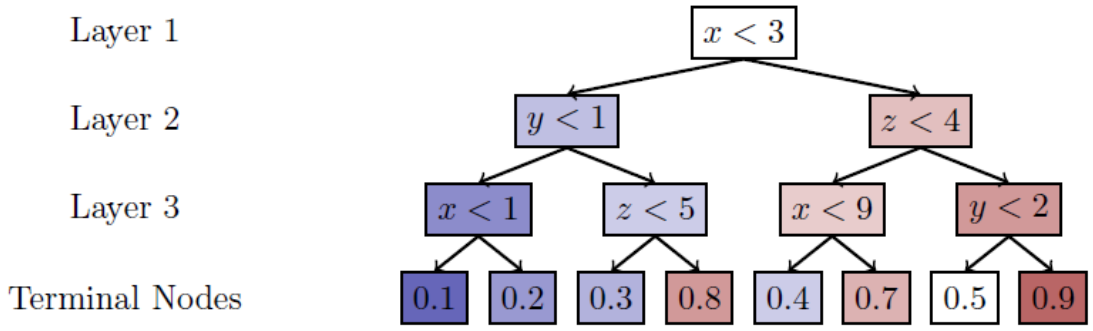

Figure 3.1: The schematic diagram of Decision Tree.

The maximum number of consecutive cuts is defined as the depth of the tree. It is a hyper-parameter. The depth of the tree is used to control the complexity and reduce the risk of over-fitting. However, Decision Trees are weak classifiers since they are sensible to many details in the training data and may be affected by finite-sample effects. The Boosted Decision Tree (BDT) constructs a stronger classification model with constructing shallow decision trees during the fitting-phase sequentially. Additional hyper-parameters, such as the number of trees and the learning rate, also referred to as shrinkage, are needed to control the complexity of the algorithm.

FastBDT determines the cuts for all nodes and all features in the same layer of the tree simultaneously by using an array of structs memory layout. There are non-uniform memory access and some sources of conditional jumps having to be considered in FastBDT, like multiple nodes per layer, signal and background, and stochastic sub-sampling. In short, FastBDT supplys an optimized implementation of the BDT algorithm that have a shorter execution time.

3.3 Training

3.3.1 Training Method

The method of training is FastBDT in basf2. The associated parameters are shown in Tab. 3.1. [16]

	value
nTrees	30,000
nCuts	10
nLevels	3
shrinkage	0.01
randRatio	0.5

Table 3.1: The associated parameters of FastBDT.

There are some other tests of using nTrees with the values 1,000 and 10,000. Nevertheless, the MVA distribution shape of signal would much separate from the shape of background with the value of nTrees 30,000. If the value of nTrees is over 30,000, the difference of the result will not be significant. There are also some other tries of using nLevels with the values 6 and 8. The results of those tries are shown in appendix A.

The method of separating signal (K_L^0) from background is using the MC truth information. By matching MC truth, We select true K_L^0 as signal with a defined output 1 from ECL candidates and give the other matched neutral particles output 0.

3.3.2 Samples

Training Samples

All ECL candidates with neutral hadron hypothesis are selected from $10 fb^{-1}$ generic MC (including $B\bar{B}$ and $q\bar{q}$). We enhance the K_L^0 as the signal to $100 fb^{-1}$ to improve the training due to the high ratio of background.

Test Samples

The generic MC sample without K_L^0 enhanced.

3.3.3 Training Variables

The eight ECL cluster variables used for training are listed in following Tab. 3.2. We notice these variables are useful for K_L^0 identification training.

ECL variables	Abbreviation
clusterAbsZernikeMoment51	clust1
clusterE1E9	clust2
clusterAbsZernikeMoment40	clust3
clusterE9E21	clust4
clusterZernikeMVA	clust5
clusterLAT	clust6
clusterE	clust7
clusterPulseShapeDiscriminationMVA (PSD)	clust8

Table 3.2: The abbreviations of training variables.

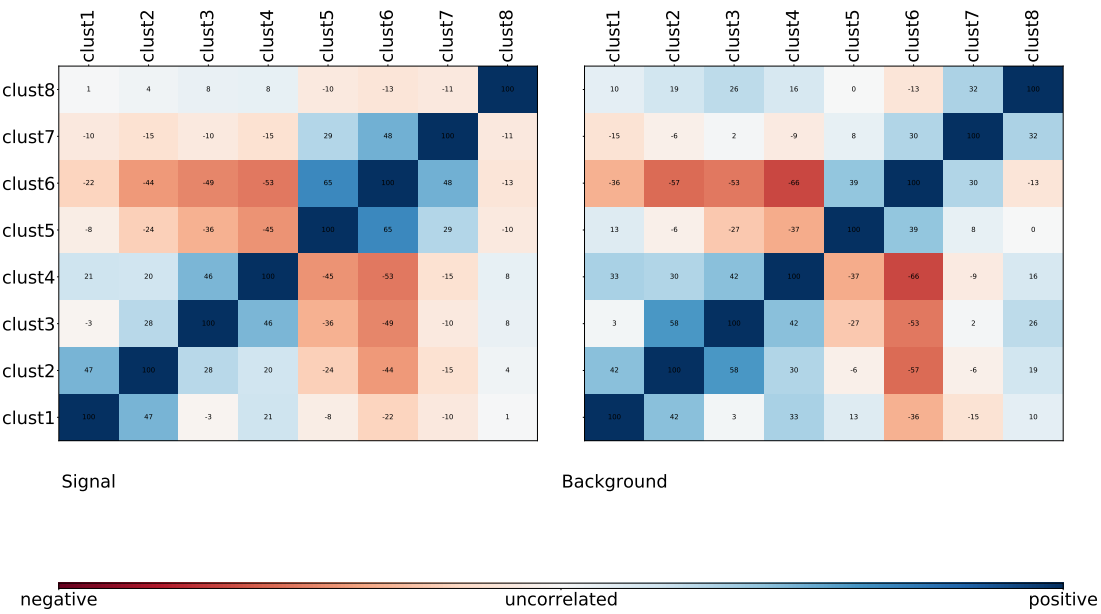

Figure 3.2: The correlation and importance of the features used in the training.

The signal and background comparisons of these ECL-based variables are shown in Fig. 3.3. The blue region is the signal, and the red region represents the background.

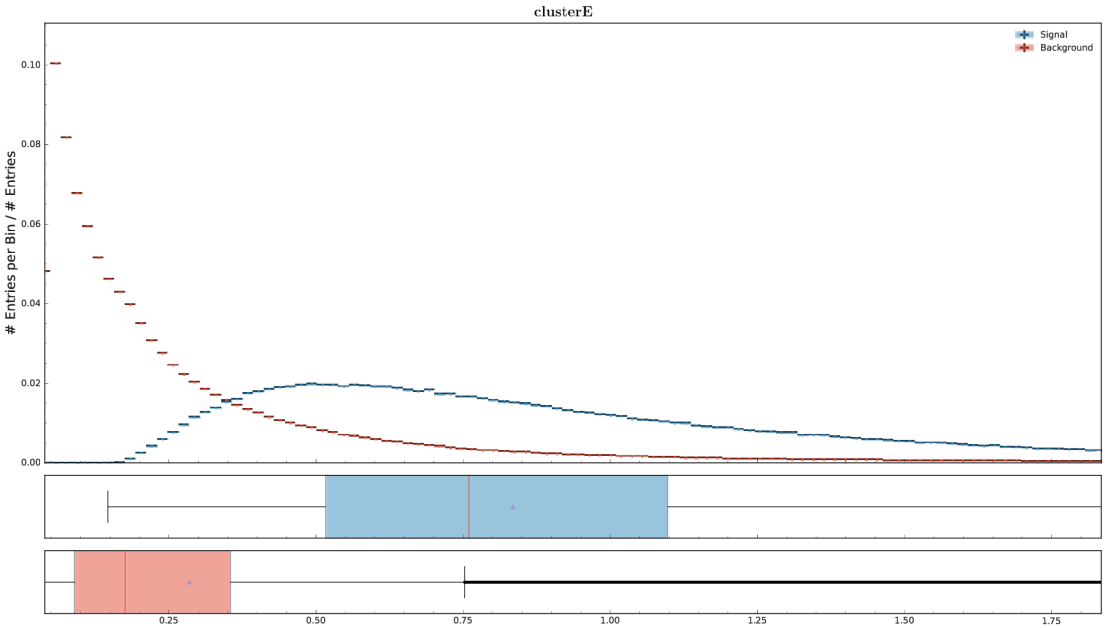

(a) clusterE

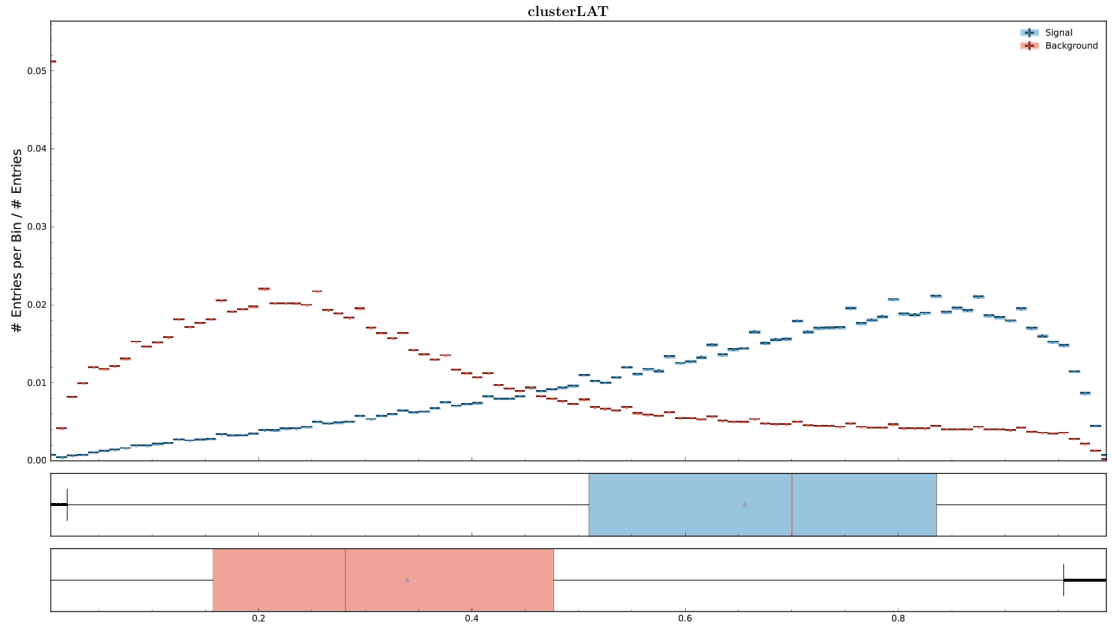

(b) clusterLAT

Figure 3.3: The distribution of the training variables. (a) clusterE (b) clusterLAT

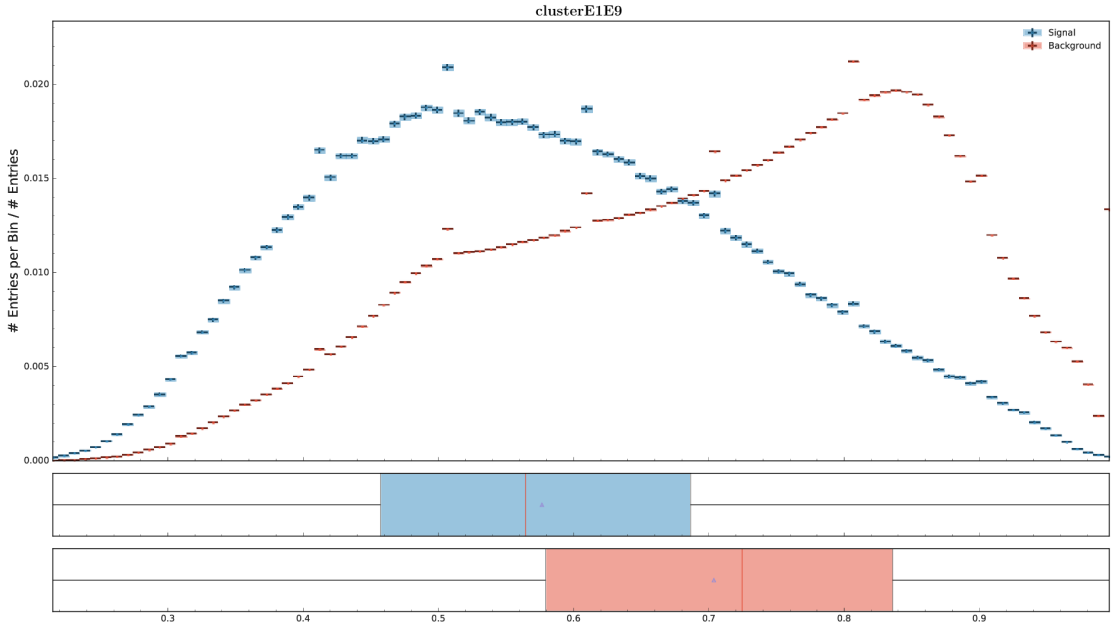

(c) clusterE1E9

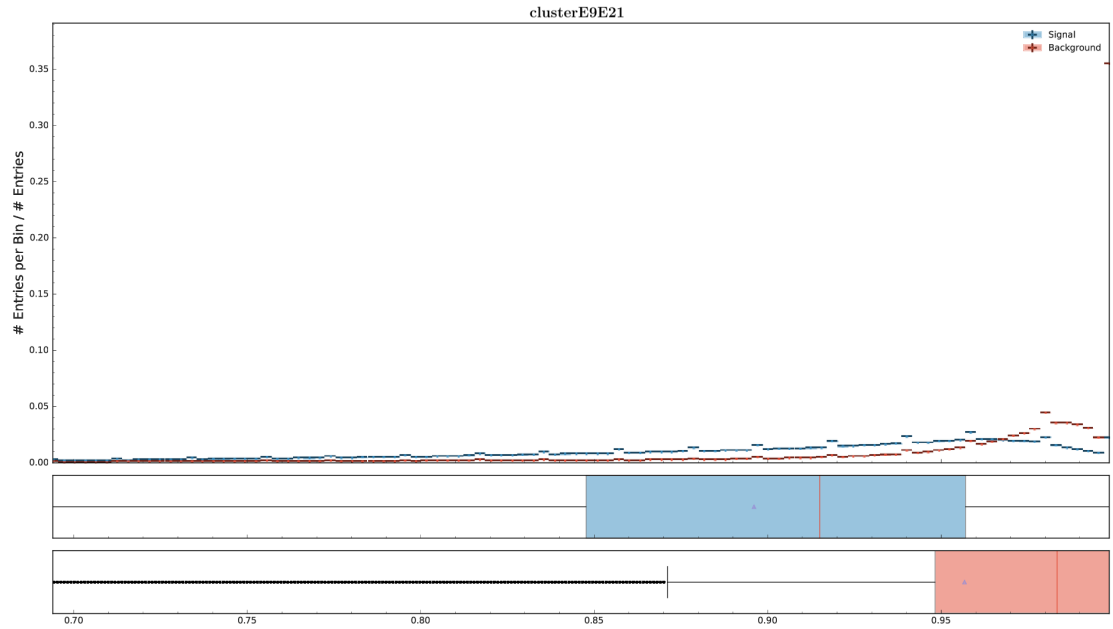

(d) clusterE9E21

Figure 3.3: The distribution of the training variables. (c) clusterE1E9 (d) clusterE9E21

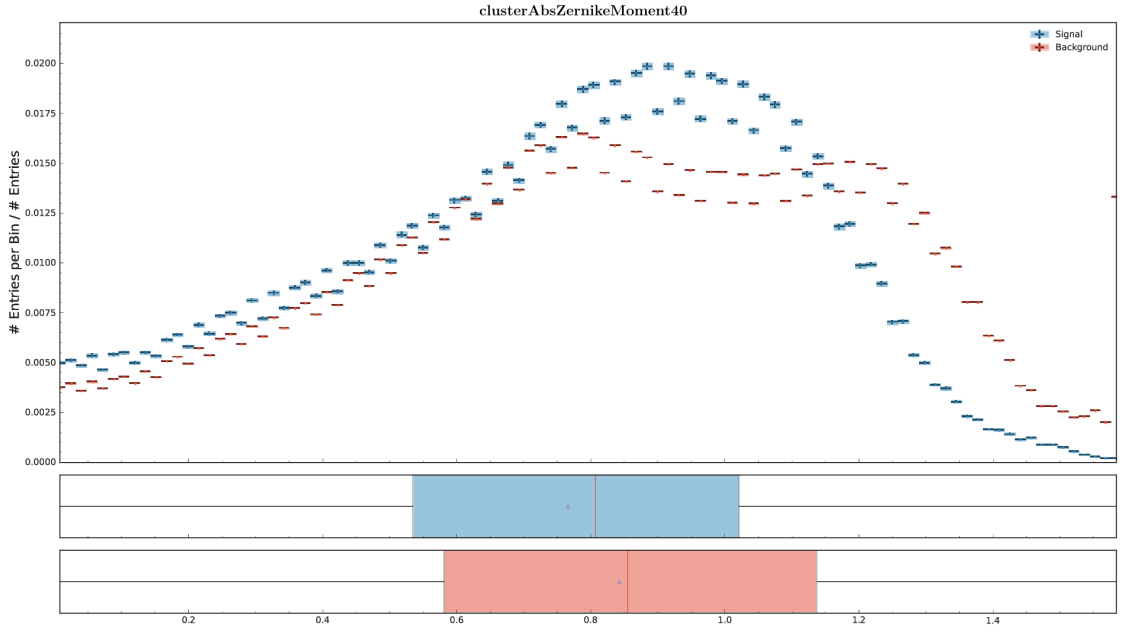

(e) clusterAbsZernikeMoment40

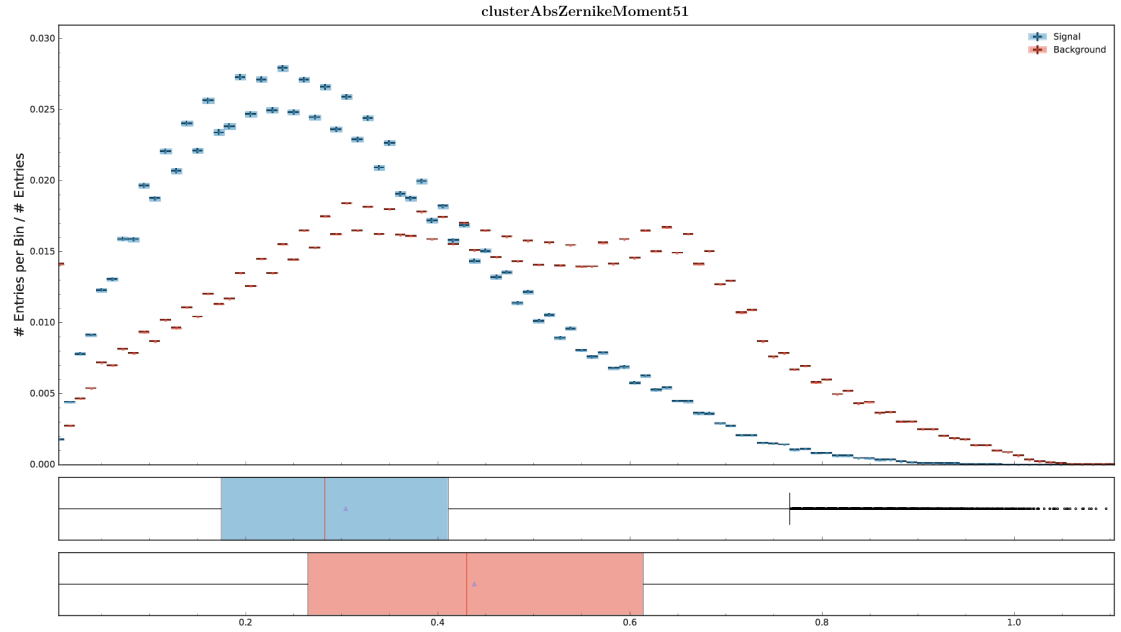

(f) clusterAbsZernikeMoment51

Figure 3.3: The distribution of the training variables. (e) clusterAbsZernikeMoment40 (f) clusterAbsZernikeMoment51

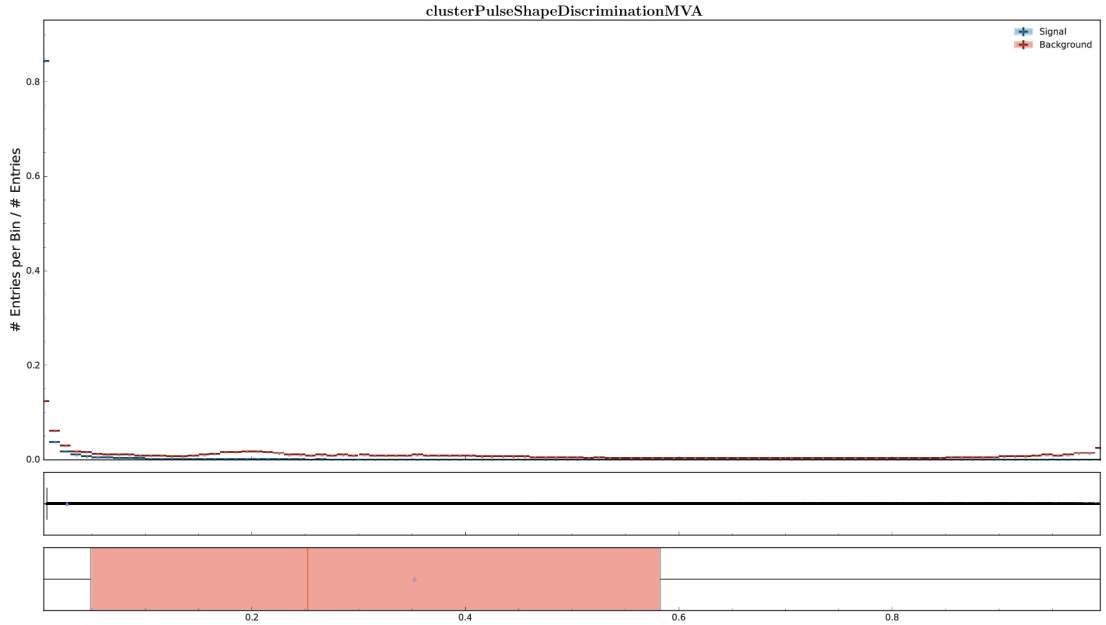

(g) clusterPulseShapeDiscriminationMVA

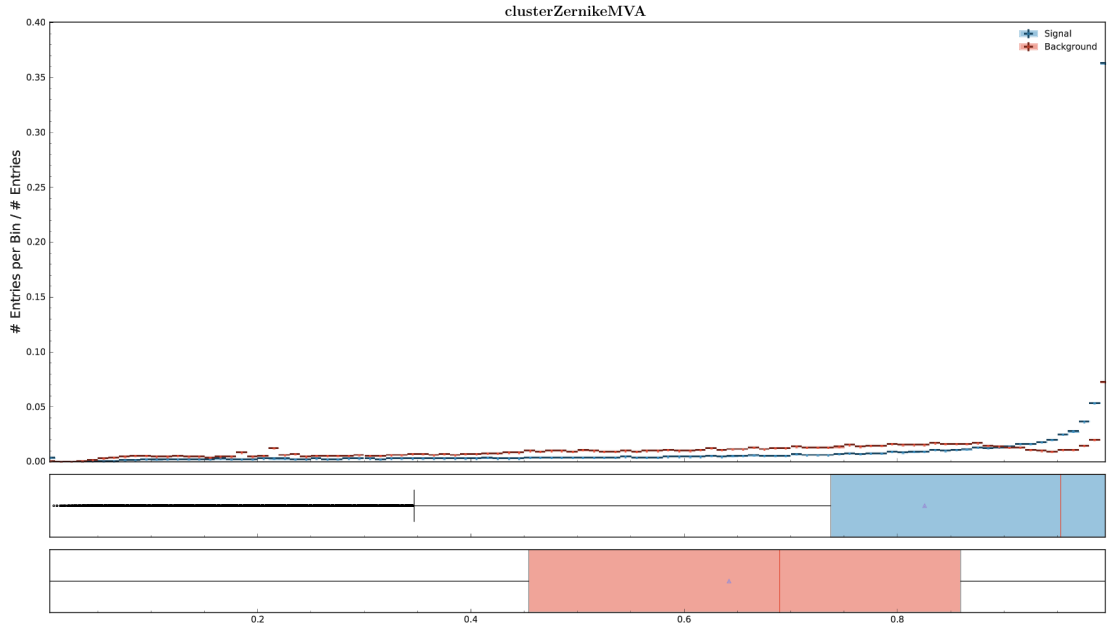

(h) clusterZernikeMVA

Figure 3.3: The distribution of the training variables. (g) clusterPulseShapeDiscriminationMVA (h) clusterZernikeMVA

K_L^0 looks different from background obviously in some variables, such as clusterE, clusterLAT, and clusterE1E9. The others are not as clear, nevertheless, they will still affect the result of training.

Here are the descriptions of these variables:

clusterE: The ECL cluster's energy corrected for leakage and background.

clusterLAT: The lateral energy distribution.

clusterE1E9: The ratio of energies of the central crystal (E1) and 3x3 crystals (E9) around the central crystal.

clusterE9E21: The ratio of energies in inner 3x3 crystals (E9) and 5x5 crystals around the central crystal without corners.

clusterAbsZernikeMoment40: The absolute value of Zernike moment 40.

clusterAbsZernikeMoment51: The absolute value of Zernike moment 51.

clusterPulseShapeDiscriminationMVA: The MVA classifier that uses pulse shape discrimination to identify electromagnetic v.s. hadronic showers.

clusterZernikeMVA: The output of a MVA using eleven Zernike moments of the cluster.

3.4 Training Results

The MVA distributions of K_L^0 in training sample and test sample are shown in Fig. 3.4 and Fig. 3.5, as γ is the major background comparing to other neutral particles. Most of K_L^0 (true K_L^0) can be recognized as signal with peak near MVA equals 1. On the other hand, EM background (true γ) is also well recognized with peak near MVA close to 0.

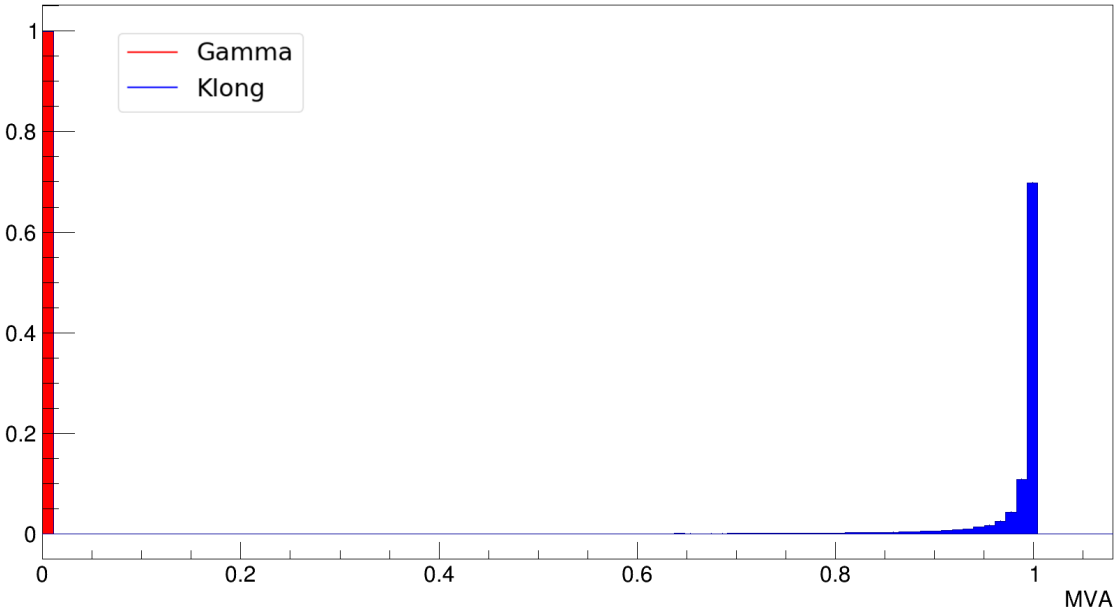

Figure 3.4: The MVA distribution of training sample.

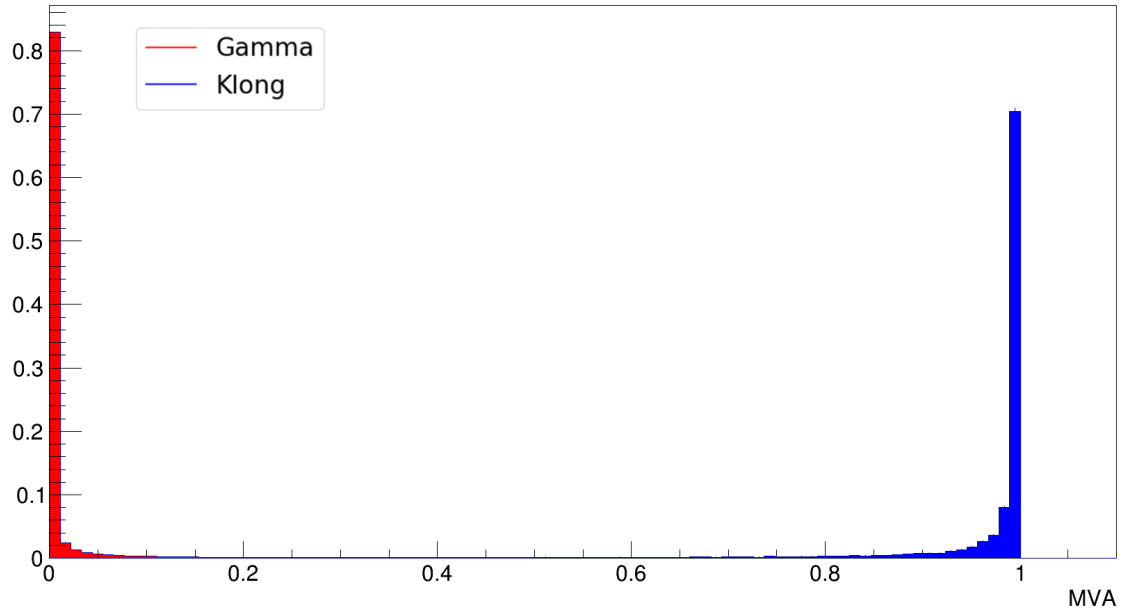

Figure 3.5: The MVA distribution of test sample.

The receiver operating characteristic (ROC) curve is a kind of indicator that is useful to understand the effect of the training. This curve can be plotted from the MVA distribution. The ROC curves for some neutral particles are shown in Fig. 3.6. γ is separated into several section by its energy. The γ with energy lager than 1 GeV is called "gammaH". The γ with energy lager than 0.5 GeV and less than 1 GeV is named "gammaM". The γ with energy between 0.1 GeV and 0.5 GeV is classified as "gammaL" and the γ with energy lower than 0.1 GeV is classified as "gammaEL". In the following Tab. 3.3, the compositions of background are listed, with their corresponding descriptions.

Particles	Note
Neutron	
Antineutron	
gammaH	mcE $>$ 1 GeV
gammaM	0.5 GeV $<$ mcE $\leq$ 1 GeV
gammaL	0.1 GeV $<$ mcE $\leq$ 0.5 GeV
gammaEL	mcE $\leq$ 0.1 GeV
other	Background particles excluding the particles above

Table 3.3: The background particles.

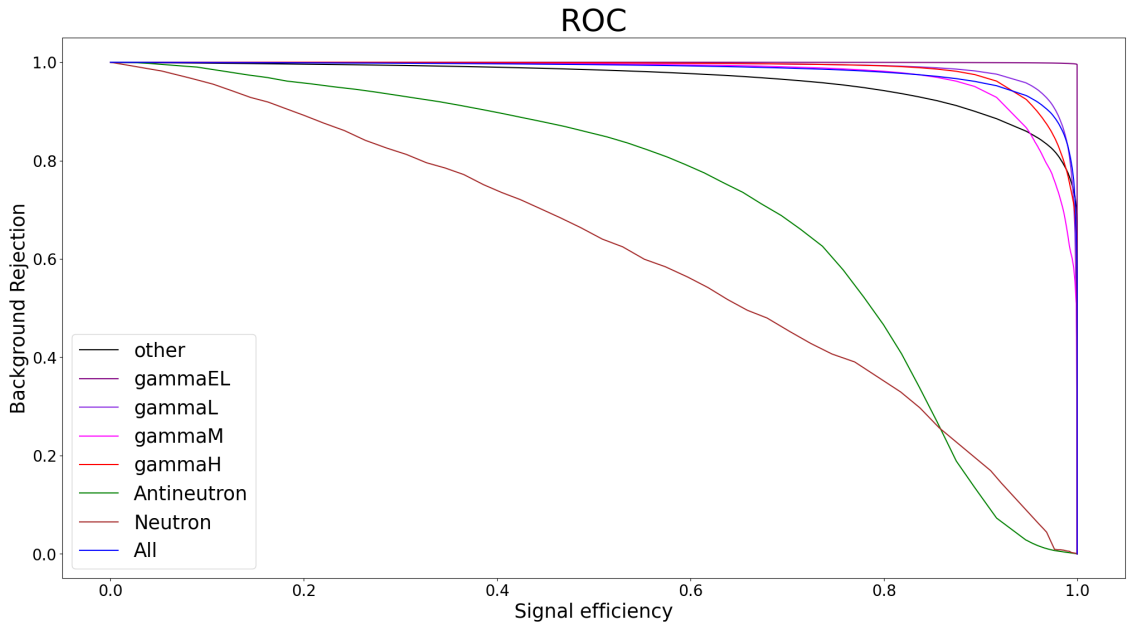

Figure 3.6: The ROC curve. (Test sample)

In this plot, for example, the green curve means K_L^0 is defined as signal and antineutron is defined as background. This curve represents that how many K_L^0s will remain and how many antineutrons will be rejected. For the blue curve, it shows that this MVA method can separate K_L^0 from background with a MVA cut. Despite it can not differentiate K_L^0 from neutron and antineutron perfectly, it still can distinguish K_L^0 from the major background, γ.

Chapter 4 The $B^0 \to J/\psi K_L^0$ Decay with ECL

The $B^0 \to J/\psi K_L^0$ decay is the decay channel for the precision measurements of CP-violation in the B sector. In this chapter, we reconstruct the $B^0 \to J/\psi K_L^0$ decay to check the result of applying MVA method on the decay mode. We estimate the selection efficiency by using the signal MC about $B^0 \to J/\psi K_L^0$ decay, where $J/\psi \to \mu^+\mu^-$. In addition, we check the number of signal in 100 fb^{-1} of generic events (including $B\bar{B}$ and $q\bar{q}$) and in the 189.049 fb^{-1} of dataset has been collected at Belle II from 2019 to 2021. [17]

4.1 Event Selection

4.1.1 J/ψ selection

The signal candidates are selected by reconstructing $J/\psi \to \mu^+\mu^-$ events first. The J/ψ particle is reconstructed from standard muons in basf2. The standard muons are with the following default cuts:

1. muonID $>$ 0.5
2. thetaInCDCAcceptance
3. nCDCHits $>$ 20
4. dr $<$ 0.5
5. abs(dz) $<$ 2

The $J/\psi \to \mu^+\mu^-$ decay needs the invariant mass of the J/ψ candidate that is consistent with the PDG value of J/ψ. We cut the mass of J/ψ that 3.06 GeV/c^2 $< m_{J/\psi} <$ 3.12 GeV/c^2 for the mass selection. The mass of J/ψ in both signal MC and generic MC is shown in Fig. 4.1 and Fig. 4.2.

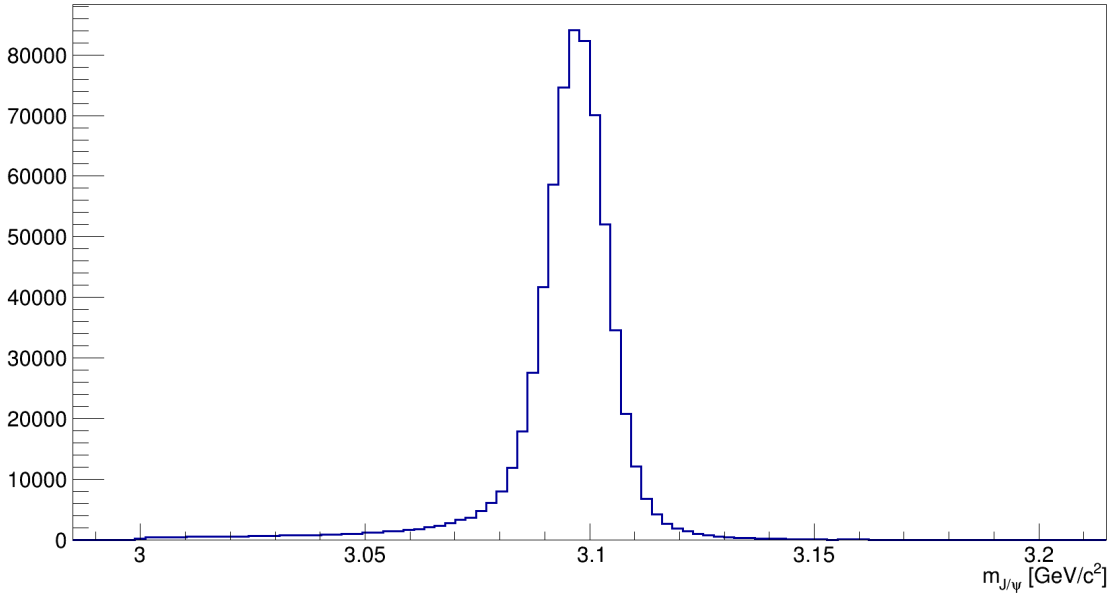

Figure 4.1: The mass of J/ψ in the signal MC. (For ECL)

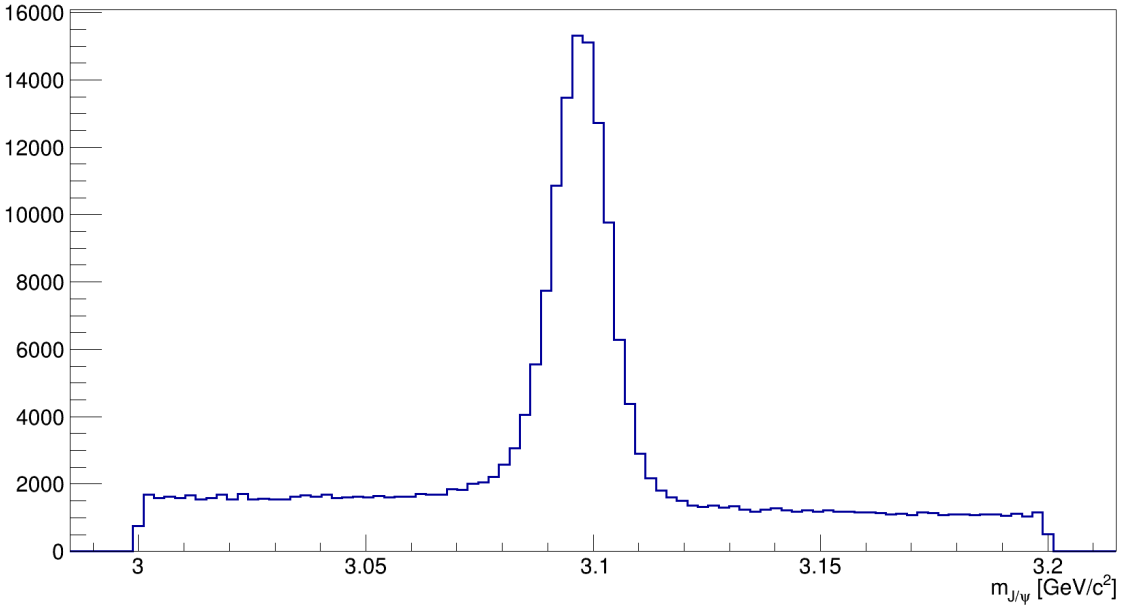

Figure 4.2: The mass of J/ψ in the generic MC. (For ECL)

4.1.2 K_L^0 selection

The K_L^0 mesons can be measured in the ECL and KLM detector. We only consider about the neutral cluster from ECL here. The variable MVA, as the identification of K_L^0, is the output of the multivariate analysis method based on Fast boosted decision tree. The MVA distribution of all K_L^0 candidates in both signal MC and generic MC are shown in Fig. 4.3 and Fig. 4.4. We select K_L^0 MVA lager than 0.8 for our K_L^0 candidates since the neutral cluster with true K_L^0 matching in signal MC is in the region where MVA > 0.8.

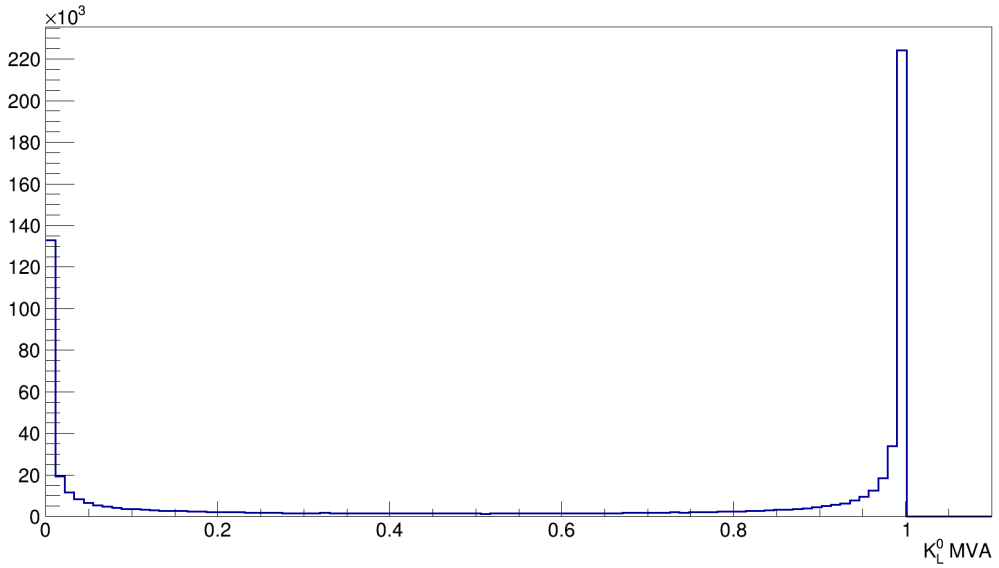

Figure 4.3: The MVA distribution of all K_L^0 candidates in the signal MC.

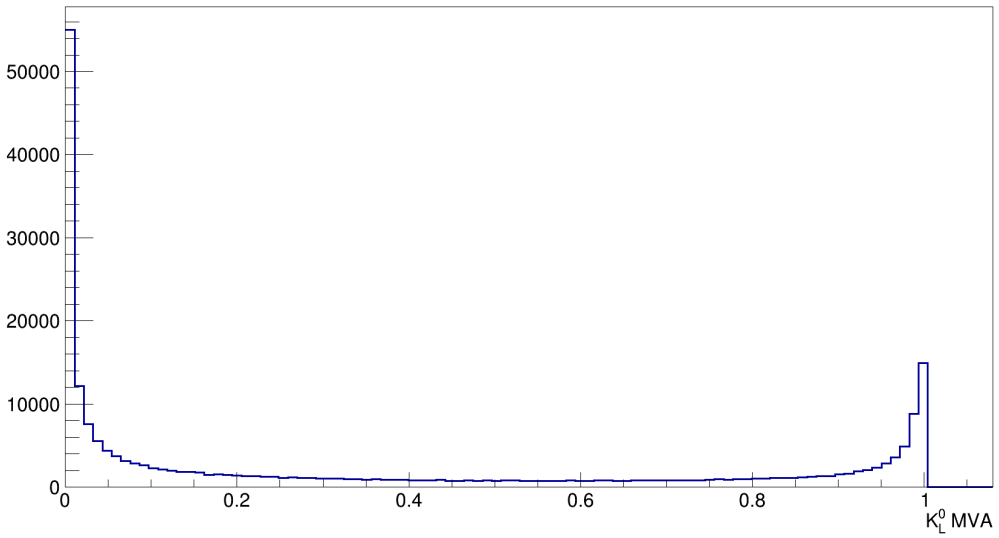

Figure 4.4: The MVA distribution of all K_L^0 candidates in the generic MC.

4.1.3 B^0 best candidate

There may be several candidates for an event. If we do not choose one candidate for one event, we will have a wrong value of efficiency. Therefore, we select the B^0 with the largest K_L^0 MVA value for best candidate.

4.2 B^0 mass constraint

The energy of K_L^0 in the ECL is a not usable measurement, but we can use the measured direction of K_L^0. Hence, we are able to calculate the momentum of the K_L^0 candidate from its direction and the reconstructed momentum of J/ψ. The requirement is constrainting the mass of B^0. We define the mass of B^0 as its PDG value, $m_{B^0} \equiv 5.279$ GeV/c^2.

From conservation of four-momentum, we know that

$$E_{K_L^0}^2 = m_{K_L^0}^2 + p_{K_L^0}^2 \tag{4.1}$$

and

$$\left(E_{J/\psi} + E_{K_L^0}\right)^2 = m_{B^0}^2 + \left(\vec{p}_{J/\psi} + \vec{p}_{K_L^0}\right)^2. \tag{4.2}$$

After solving the equations, we get

$$p_{K_L^0} = \frac{\Delta m^2 \left(\vec{p}_{J/\psi} \cdot \hat{p}_{K_L^0}\right) \pm E_{J/\psi}\sqrt{\left(\Delta m^2\right)^2 - 4m_{K_L^0}^2\left(E_{J/\psi}^2 - \left(\vec{p}_{J/\psi} \cdot \hat{p}_{K_L^0}\right)^2\right)}}{2\left(E_{J/\psi}^2 - \left(\vec{p}_{J/\psi} \cdot \hat{p}_{K_L^0}\right)^2\right)}, \tag{4.3}$$

where

$$\Delta m^2 \equiv m_{B^0}^2 - m_{J/\psi}^2 - m_{K_L^0}^2. \tag{4.4}$$

Then, we can get the energy of K_L^0 using eq. (4.1) with the momentum of K_L^0 in eq. (4.3) we get.

Since there is the end point problem in ΔE fitting, we choose another variable, p_B^*, which is better in fitting. p_B^* is the momentum of B^0 in center-of-mass (CoM) frame. We transform the energy of K_L^0 from lab frame to CoM frame,

$$E_{K_L^0}^* = \gamma \left(E_{K_L^0} - \left(\vec{\beta} \cdot \hat{p}_{K_L^0} \right) p_{K_L^0} \right), \tag{4.5}$$

where

$$\gamma = \frac{1}{\sqrt{1 - \frac{\vec{v}^2}{c^2}}}, \quad \vec{\beta} = \frac{\vec{v}}{c}, \tag{4.6}$$

and $\vec{v}$ is the velocity of K_L^0. Then,

$$p_B^* \equiv \sqrt{\left(E_{J/\psi}^* + E_{K_L^0}^* \right)^2 - m_{B^0}^2}. \tag{4.7}$$

4.3 The results

4.3.1 $B^0 \to J/\psi K_L^0$ decay in signal MC

In one million events of $B^0 \to J/\psi K_L^0$ ($J/\psi \to \mu+\mu-$) decay using signal MC, the signal peak is obvious. With the selections, where 3.06 GeV/c^2 $< m_{J/\psi} <$ 3.12 GeV/c^2 and K_L^0 MVA lager than 0.8, there are 252,099 candidates. The total efficiency is about 25% as shown in Fig. 4.5. The muon selection efficiency is 67 %, it indicates about 80 % each muon. The K_L^0 selection efficiency is about 50%. Moreover, the efficiency of J/ψ mass selection is roughly 96 % and the efficiency of p_B^* signal region selection is roughly 75 %.

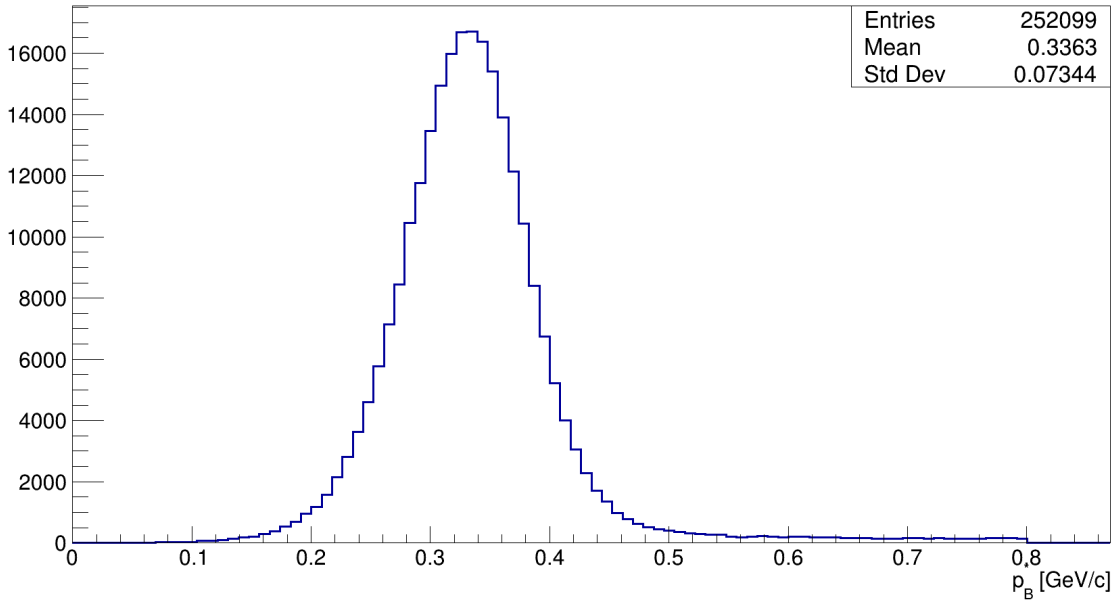

Figure 4.5: The p_B^* distribution with the one million events signal MC.

4.3.2 $B^0 \to J/\psi K_L^0$ decay in generic MC

We check the p_B^* in 100 fb^{-1} generic MC (including $B\bar{B}$ and $q\bar{q}$) as well. The numbers of $B\bar{B}$ events is 1.02×10^8. With the same selections, the signal peak is clear to see. As shown in Fig. 4.6, there are 681 ± 71 signals and 3059 ± 86 backgrounds. We model the p_B^* distribution of signal with a Gaussian probability density function (PDF) and model the p_B^* distribution of background with a Chebyshev polynomials PDF.

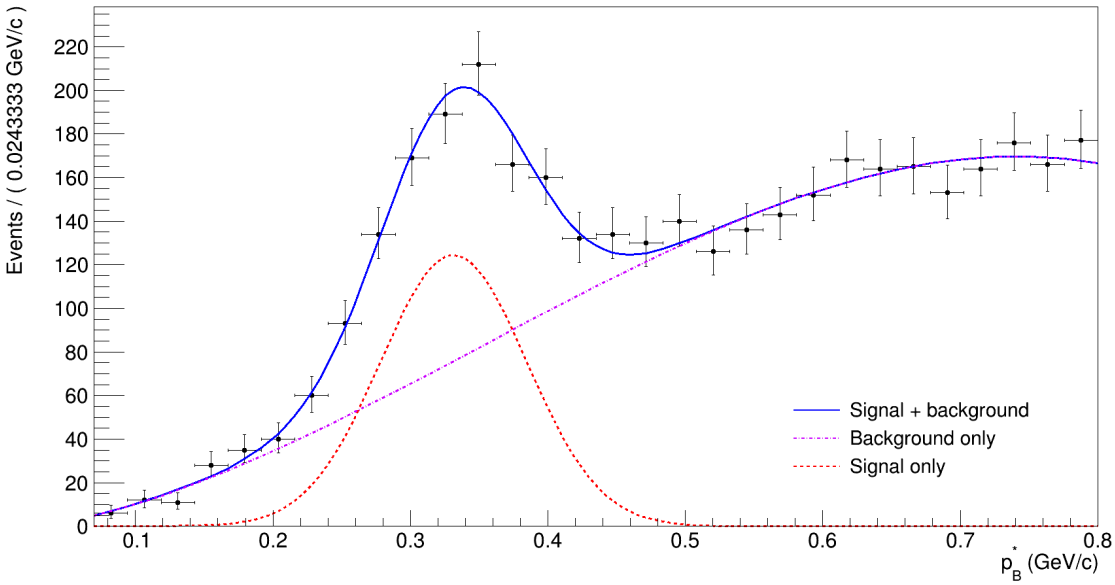

Figure 4.6: The p_B^* distribution with the 100 fb^{-1} generic MC.

4.3.3 The validation

From PDG, the Branching Fraction of $B^0 \to J/\psi K^0$ is 8.91×10^{-4}, and the Branching Fraction of $J/\psi \to \mu + \mu-$ is 5.961×10^{-2}. [7] Hence, the Branching Fraction of $B^0 \to J/\psi K^0_L$, in which $J/\psi \to \mu + \mu-$, is about

$$8.91 \times 10^{-4} \times 5.961 \times 10^{-2} \times 0.5 = 2.66 \times 10^{-5}, \tag{4.8}$$

where 0.5 is approximately the probability of $K^0 \to K^0_L$.

Assume the K^0_L mesons are all from ECL cluster, the signals we get divided by the selection efficiency and the numbers of $B\bar{B}$ events. The Branching Fraction is

$$\begin{aligned} &\frac{\text{signals}}{\text{the numbers of } B\bar{B} \text{ events}} \div \text{selection efficiency} \\ =&\frac{(681 \pm 71)}{1.02 \times 10^8} \div \left(2.52 \times 10^{-1}\right) = (2.65 \pm 0.28) \times 10^{-5}. \end{aligned} \tag{4.9}$$

From eq. (4.8) and eq. (4.9), the result from MC is close to the prediction.

4.3.4 $B^0 \to J/\psi K^0_L$ decay in Data

We determine the numbers of signal and background about $B^0 \to J/\psi K^0_L$ decay with 189.049 fb^{-1} Belle II dataset in the interval of p^*_B from 0 GeV to 0.8 GeV. As we do in generic MC, we model the p^*_B distribution of signal with a Gaussian PDF and model the p^*_B distribution of background with a Chebyshev polynomials PDF. The results are $N_{sig} = 1031 \pm 95$ and $N_{bkg} = 3269 \pm 106$, as shown in Fig. 4.7.

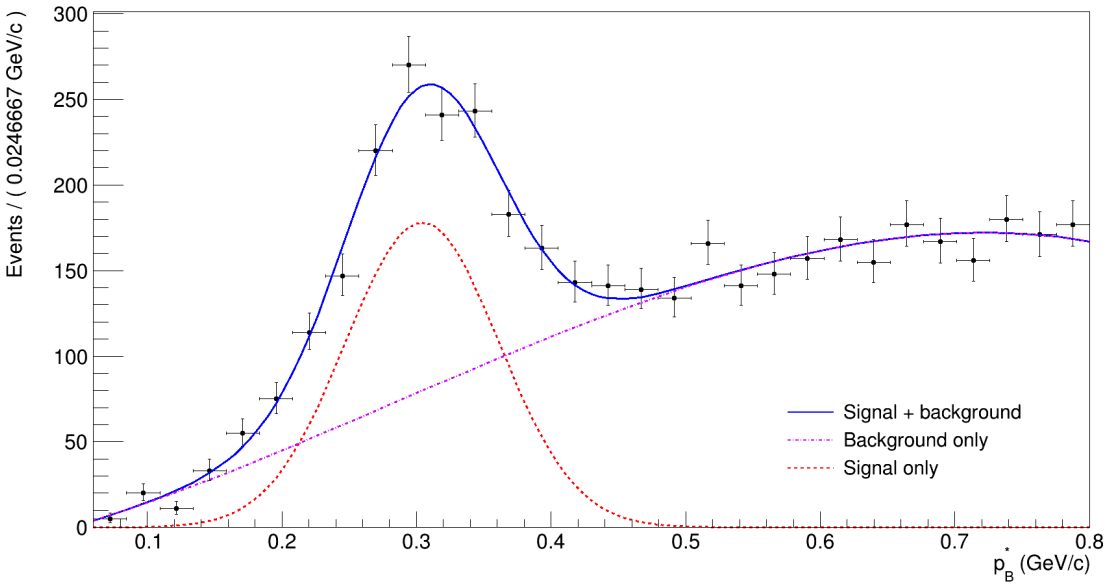

Figure 4.7: The p_B^* distribution with the 189.049 fb^{-1} dataset.

Although the rate of signal in data ($\frac{1031\pm95}{189.049fb^{-1}} \approx 5.45$ signals per fb^{-1}) is lower than the one in generic MC ($\frac{681\pm71}{100fb^{-1}} \approx 6.81$ signals per fb^{-1}), the ratio of signal to background in data ($\frac{1031\pm95}{3269\pm106} \approx 31.5\%$) is higher than the one in generic MC ($\frac{681\pm71}{3059\pm86} \approx 22.3\%$).

Chapter 5 The $B^0 \to J/\psi K_L^0$ Decay with KLM and Comparison

The K_L^0 particles are measurable in ECL and KLM cluster. We reconstruct the $B^0 \to J/\psi K_L^0$ decay with only ECL information in Chapter 4. In this chapter, we consider the KLM case. We reconstruct the $B^0 \to J/\psi K_L^0$ decay with only KLM information. The event selections and reconstruct method are based on [18]. There are some differences due to the unknown factors. In addition, we compare the results of both ECL and KLM case briefly to check the overlap of them.

5.1 Event Selection

5.1.1 J/ψ selection

The J/ψ candidate selection is similar to the one in Chapter 4. The J/ψ particle is reconstructed from standard muons in basf2. The selection of the J/ψ mass is consistent with the PDG value that 3.06 GeV/c^2 $< m_{J/\psi} <$ 3.12 GeV/c^2. The mass of J/ψ in both signal MC and generic MC is shown in Fig. 5.1 and Fig. 5.2. The distributions of J/ψ mass are similar to those in Chapter 4.

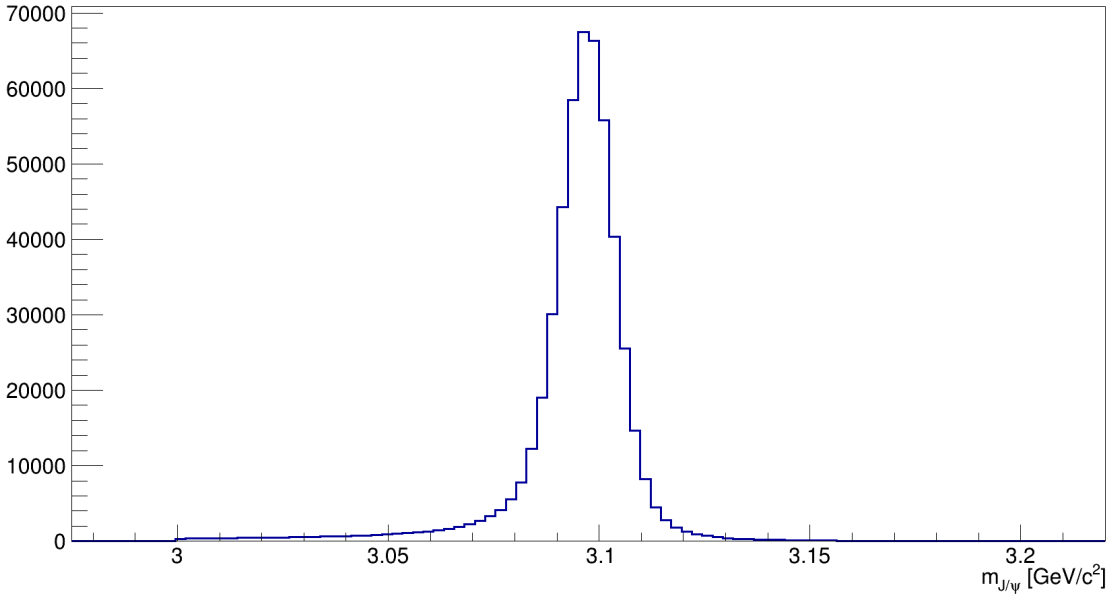

Figure 5.1: The mass of J/ψ in the signal MC. (For KLM)

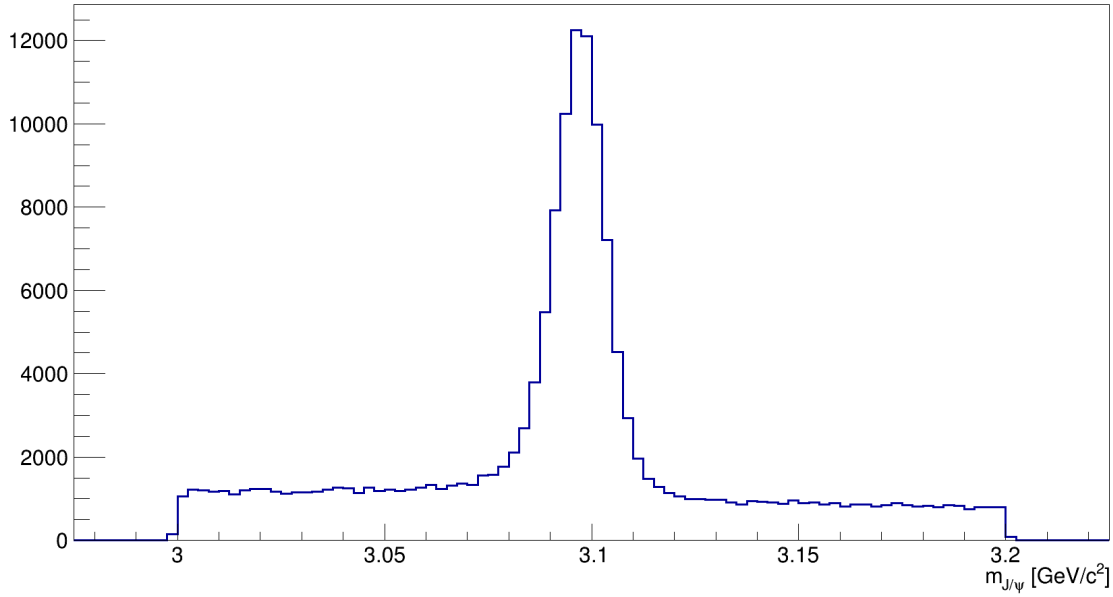

Figure 5.2: The mass of J/ψ in the generic MC. (For KLM)

5.1.2 K_L^0 selection

We only consider the neutral cluster from KLM here. The variable **klmClusterKlId** is the output of the multivariate analysis method based on boosted decision tree. The MVA distribution of all K_L^0 candidates in both signal MC and generic MC are shown in Fig. 5.3 and Fig. 5.4

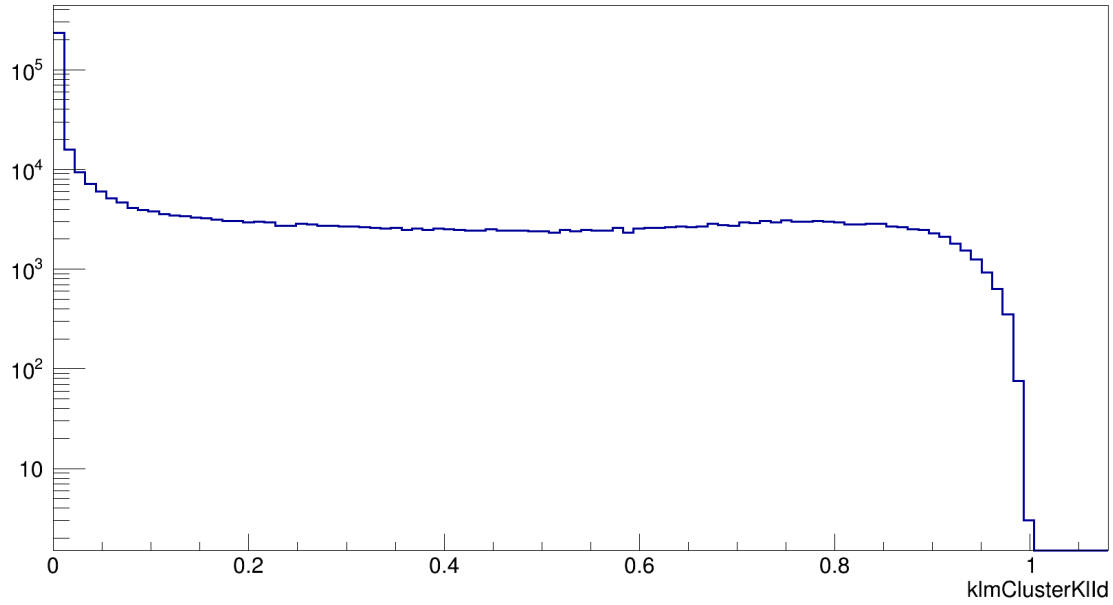

Figure 5.3: The **klmClusterKlId** distribution of all K_L^0 candidates in the signal MC.

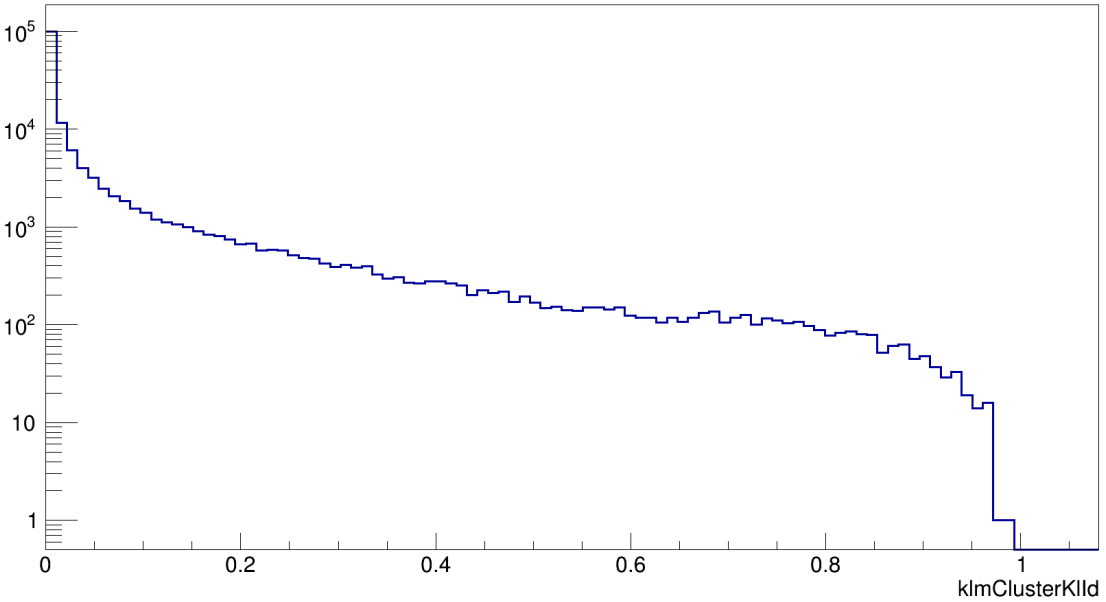

Figure 5.4: The **klmClusterKlId** distribution of all K_L^0 candidates in the generic MC.

Based on [18], we select **klmClusterKlId** ≥ 0.25 for our K_L^0 candidates. Moreover, in order to eliminate spurious clusters and make the signal shape much clear, we apply the requirement $N_{layers} \geq 2$ explicitely.

5.1.3 B^0 best candidate

We still need to choose one candidate for one event in order to avoid having a wrong value of efficiency. Hence, we select the largest value of **klmClusterKlId** for B^0 best candidate.

5.2 The results

We constraint the mass of B^0 and use the measured direction of K_L^0 to calculate the momentum of the K_L^0 candidate.

5.2.1 $B^0 \to J/\psi K_L^0$ decay in signal MC

With the selections, where 3.06 GeV/$c^2 < m_{J/\psi} <$ 3.12 GeV/c^2, K_L^0 **klmClusterKlId** $\geq$ 0.25, and $N_{layers} \geq 2$, there are 86,825 candidates in one million events signal MC of $B^0 \to J/\psi K_L^0$ ($J/\psi \to \mu + \mu-$) decay. The efficiency is about 8.7% as shown in Fig. 5.5.

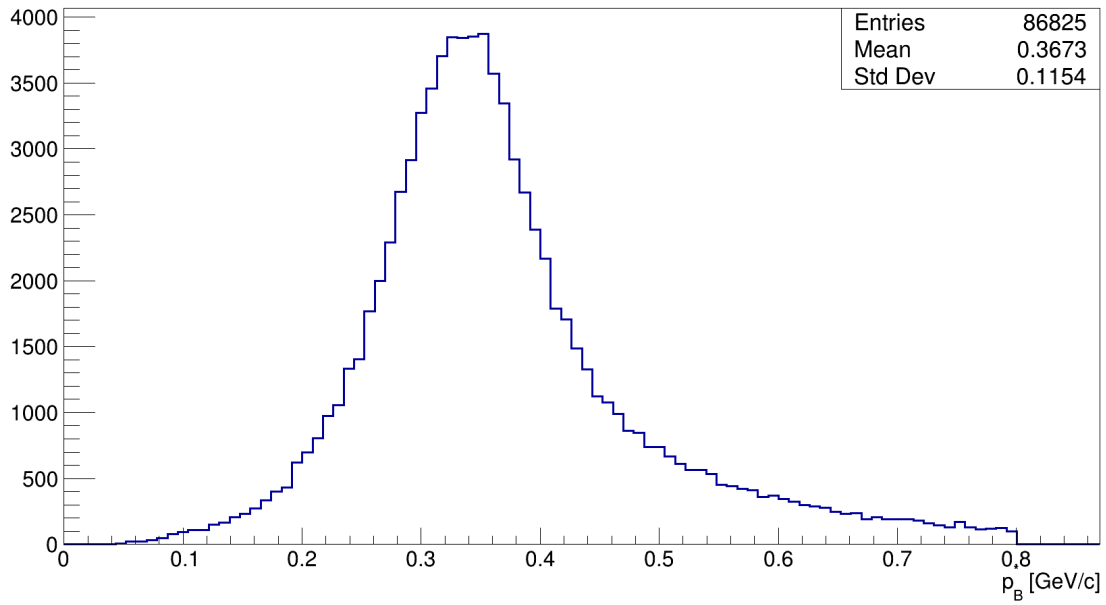

Figure 5.5: The p_B^* distribution with the one million events signal MC in KLM case.

5.2.2 $B^0 \to J/\psi K_L^0$ decay in generic MC

In 100 fb^{-1} generic MC (including $B\bar{B}$ and $q\bar{q}$), the numbers of $B\bar{B}$ events is 1.02×10^8. With the same selections, there are 185 ± 38 signals and 562 ± 43 backgrounds, as shown in Fig. 5.6. We model the p_B^* distribution of signal with a Gaussian PDF and model the background with a Chebyshev polynomials PDF.

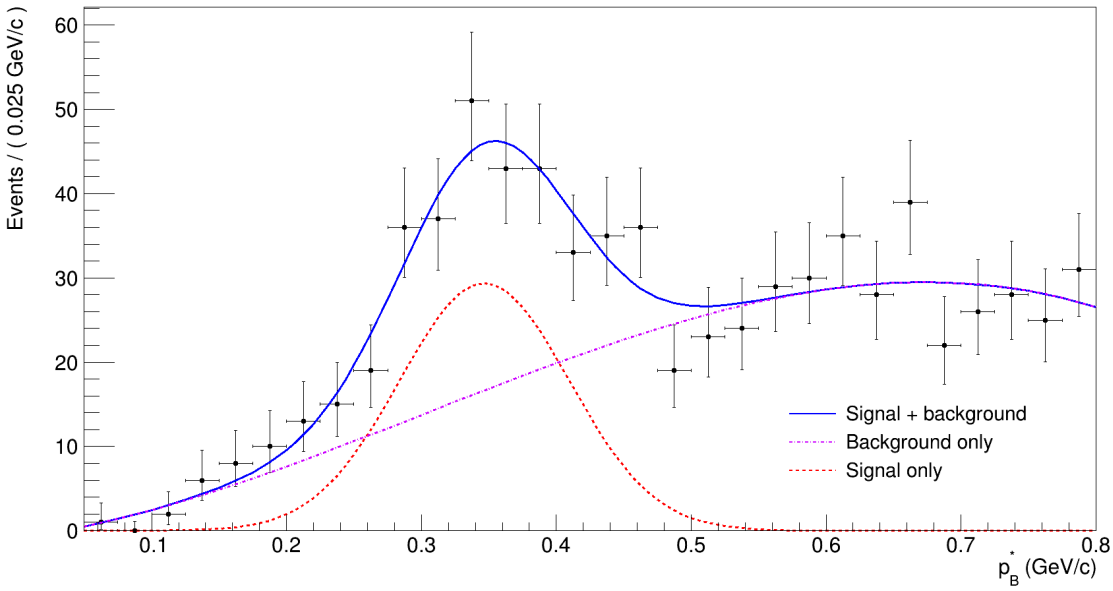

Figure 5.6: The p_B^* distribution with the 100 fb^{-1} generic MC in KLM case.

5.2.3 The validation

The Branching Fraction of $B^0 \to J/\psi K_L^0$, in which $J/\psi \to \mu + \mu -$, is about

$$8.91 \times 10^{-4} \times 5.961 \times 10^{-2} \times 0.5 = 2.66 \times 10^{-5}, \tag{5.1}$$

as written in Chapter 4.

Assume the K_L^0 mesons are all from KLM cluster, the signals we get divided by the selection efficiency and the numbers of $B\bar{B}$ events. The Branching Fraction is

$$\begin{aligned} &\frac{\text{signals}}{\text{the numbers of } B\bar{B} \text{ events}} \div \text{selection efficiency} \\ =&\frac{(185 \pm 38)}{1.02 \times 10^8} \div \left(8.68 \times 10^{-2}\right) = (2.09 \pm 0.43) \times 10^{-5}. \end{aligned} \tag{5.2}$$

From eq. (4.9) and eq. (5.2), the Branching Fraction of $B^0 \to J/\psi K_L^0$ we get in KLM case is lower than the one we get in ECL case.

5.2.4 $B^0 \to J/\psi K_L^0$ decay in Data

We determine the numbers of signal and background about $B^0 \to J/\psi K_L^0$ decay with 189.049 fb^{-1} Belle II dataset in the interval of p_B^* from 0 GeV to 0.8 GeV. We model the p_B^* distribution of signal with a Gaussian PDF and model the p_B^* distribution of background with a Chebyshev polynomials PDF as we do in generic MC. The results are $N_{sig} = 309 \pm 67$ and $N_{bkg} = 735 \pm 70$, as shown in Fig. 5.7.

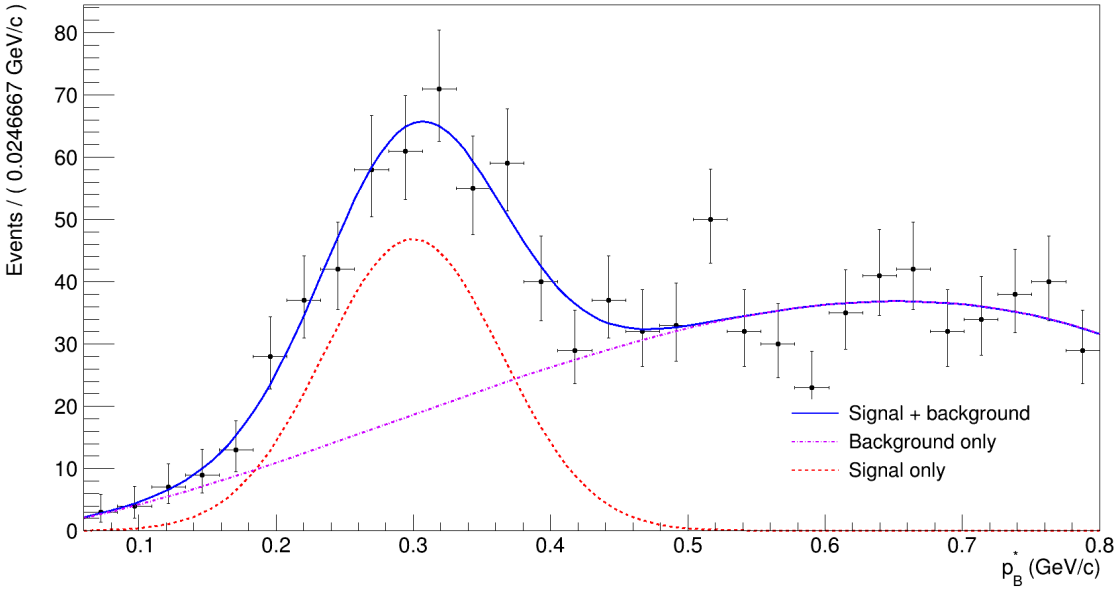

Figure 5.7: The p_B^* distribution with the 189.049 fb^{-1} dataset in KLM case.

Similar to the ECL case, the rate of signal in data ($\frac{309\pm67}{189.049 fb^{-1}} \approx 1.63$ signals per fb^{-1}) is lower than the one in generic MC ($\frac{185\pm38}{100 fb^{-1}} \approx 1.85$ signals per fb^{-1}), the ratio of signal to background in data ($\frac{309\pm67}{735\pm70} \approx 42\%$) is higher than the one in generic MC ($\frac{185\pm38}{562\pm43} \approx 32.9\%$) for the KLM case.

5.3 Comparison

The method to determine the overlap of the $B^0 \to J/\psi K_L^0$ decay in the ECL case and the KLM case is comparing the event ID for both case. The overlap is the event ID exists in both ECL and KLM situations, such as the green part of Fig. 5.8. Furthermore, the red part in Fig. 5.8 is the set of the event ID only exists in KLM case and the blue part is the set of the event ID only exists in ECL. In this thesis, we check the overlap in whole region and main signal region (0.2 GeV/c $< p_B^* <$ 0.4 GeV/c) with signal MC and Data.

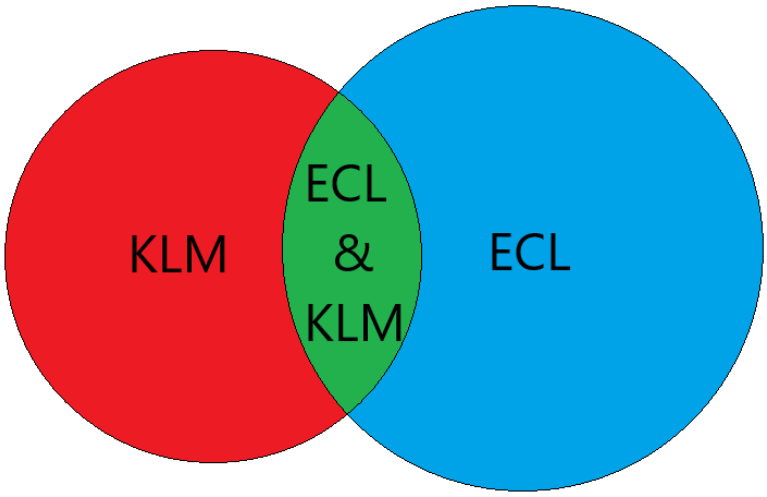

Figure 5.8: The schematic diagram of the relationship between ECL and KLM.

In signal MC, there are almost 120 thousand $B^0 \to J/\psi K_L^0$ ($J/\psi \to \mu+\mu-$) events with KLM and 340 thousand events with ECL reconstructed for the whole region. For 121,048 KLM events, 78,808 events are KLM only. For 339,254 ECL events, 297,014 events are ECL only. One third of KLM events and one eighth of ECL events have the same event ID.

In the main signal region, there are about 67 thousand $B^0 \to J/\psi K_L^0$ events with KLM and 221 thousand events with ECL reconstructed. 62,454 events are KLM only and 216,267 events are ECL only. The overlap includes 4,752 events. The results of signal MC are summerized in Tab. 5.1.

Events	Whole region	Main signal region
KLM only	78,808	62,454
Overlap	42,240	4,752
ECL only	297,014	216,267

Table 5.1: The comparison between KLM and ECL in signal MC.

In Belle II dataset, there are almost 10 thousand $B^0 \to J/\psi K_L^0$ ($J/\psi \to \mu + \mu-$) events with KLM and 40 thousand events with ECL reconstructed for the whole region. For 9,901 KLM events, 8,427 events are KLM only. For 39,962 ECL events, 38,488 events are ECL only. There are about five thousand events IDs exist in both KLM and ECL situations.

In the main signal region, there are about four hundred $B^0 \to J/\psi K_L^0$ events with KLM and 1.5 thousand events with ECL reconstructed. 396 events are KLM only and 1,577 events are ECL only. The overlap includes only 10 events. The results of data are summerized in Tab. 5.2.

Events	Whole region	Main signal region
KLM only	8,427	396
Overlap	1,474	10
ECL only	38,488	1,577

Table 5.2: The comparison between KLM and ECL in Data.

From Tab. 5.1 and Tab. 5.2, none of the number in the overlap part reaches half of the KLM or the ECL results. This shows a significant difference in the K_L^0 that reconstructed from ECL and KLM.

Chapter 6 Conclusions

The Belle II experiment is performing asymmetric energy e^+e^- collision, which allows us to probe more details in particle physics. The B meson produced in the collision provides us the oppotunity of observing the CP-violation in SM with its decay. K_L^0 meson is one of the B meson decay related particles, and its identification is significant, which is the main focus in this thesis.

The trained MVA identifier can seperate K_L^0 from γ and other neutral hadrons. With the 25% selection efficiency, we show the results of the reconstruction about the $B^0 \to J/\psi K_L^0$ decay in 100 fb^{-1} generic MC and Belle II experiment dataset with integrated luminosity of 189.049 fb^{-1}. The signal yields are:

$$N_{sig}(\text{MC}) = 681 \pm 71,$$
$$N_{sig}(\text{Data}) = 1031 \pm 95.$$

Since MC and Data have K_L^0 tagging efficiency difference, the next process can be calibrating K_L^0 tagger with $e^+e^- \to \phi\gamma$ channel. [19]

On the other hand, the reconstructing result of ECL does not have much overlap with the result of KLM. This means the K_L^0 from ECL cluster that we select for reconstructing the $B^0 \to J/\psi K_L^0$ decay is much different from the K_L^0 which is from KLM cluster. All in all, these results might give another way for K_L^0 identification.

Reference

[1] The ATLAS Collaboration. Observation of a new particle in the search for the Standard Model Higgs boson with the ATLAS detector at the LHC. *Phys.Lett. B716 (2012) 1-29*, 716(1):1–29, Sep 2012.

[2] The CMS Collaboration. Observation of a new boson at a mass of 125 GeV with the CMS experiment at the LHC. *Phys. Lett. B 716 (2012) 30*, 716(1):30–61, Sep 2012.

[3] M. Yamaga, K. Hanagaki, D. Marlow, S. Vahsen, and K. Abe. Measurement of $\sin 2\phi_1$ in $B^0 \to J/\psi K_L$ Decays. *Belle Note 358*, 2000.

[4] David Griffiths. Intriduction to Elementary Particles. *Wiley-VCH*, 2008.

[5] Mark Thomson. Modern particle physics. *Cambridge University Press*, 2013.

[6] M. Ciuchini, E. Franco, V. Lubicz, G. Martinelli, L. Silvestrini, and C. Tarantino. Power corrections to the CP-violation parameter ε_K. *JHEP*, 02:181, Feb 2022.

[7] R.L. Workman et al. Review of Particle Physics. *Prog. Theor. Exp. Phys*, 2022.

[8] Belle Collaboration. Precise measurement of the CP violation parameter $\sin 2\phi_1$ in $B^0 \to (c\bar{c})K^0$ decays. *Phys. Rev. Lett. 108, 171802 (2012)*, 108(17):171802, Apr 2012.

[9] Kazunori Akai, Kazuro Furukawa, and Haruyo Koiso. SuperKEKB Collider. *Nuclear Instruments and Methods in Physics Research Section A: Accelerators, Spectrometers, Detectors and Associated Equipment*, 907:188–199, Nov 2018.

[10] T. Abe et al. Belle II Technical Design Report. *KEK-REPORT-2010-1*, November 2010.

[11] I. Adachi, T. E. Browder, P. Križan, S. Tanaka, and Y. Ushiroda. Detectors for extreme luminosity: Belle II. *Nucl. Instrum. Meth. A*, 907:46–59, 2018.

[12] T. Kuhr, C. Pulvermacher, M. Ritter, T. Hauth, and N. Braun. The Belle II Core Software. *Comput. Softw. Big Sci. 3 (2019) no.1*, 3(1), Nov 2018.

[13] David Dossett. Computing and Software at Belle II. *EPJ Web Conf.*, 245:11007, 2020.

[14] Thomas Keck. FastBDT: A speed-optimized and cache-friendly implementation of stochastic gradient-boosted decision trees for multivariate classification. *Comput. Softw. Big Sci.*, September 2016.

[15] Valeria Fioroni. Study of charmless $B \to \eta' K$ decays with the Belle II experiment. *BELLE2-MTHESIS-2022-005*, 2022.

[16] Y.-T. Chen, K. Huang, Y.-R. Lin, J.-G. Shiu, and M.-Z. Wang. Particle Indentication of Anti-neutron. *BELLE2-NOTE-TE-2020-016*, 2020.

[17] Claudia Cecchi, Guglielmo De Nardo, Elisa Manoni, and Mario Merola. B counting measurement in "Moriond 2022/ICHEP 2022" Belle II dataset. *BELLE2-NOTE-PH-2022-007*, 2022.

[18] Belle II Collaboration. Rediscovery of $B^0 \to J/\psi K^0_L$ at Belle II. *BELLE2-CONF-PH-2021-009*, June 2021.

[19] A. Tchouvikov, K. Korotushenko, D. Marlow, and S. Vahsen. Using $e^+e^- \to \gamma\phi$ decay followed by $\phi \to K_S K_L$ for K_L calibration. *Belle Note 580*, 2002.

Appendix A

The MVA distribution of the different training results applying on the test sample

Here are the MVA distributions of training results with different parameters applying on the test sample. For nTrees is 1000 and nLevels is 3, we have figure (a). If we change the value of nLevels to 6 or 8, we will have the results as figure (b) or figure (c). If we change the value of nTrees to 10000 or 30000, we will have the results as figure (d) or figure (e). If we change both value of nLevels and nTrees to 8 and 10000, we will have the results as figure (f).

The results above are obtained from training samples with K_L^0 enhanced. The figure (g) is the trained result without K_L^0 enhanced applying on the test sample. The matched true K_L^0s in figure (g) are almost in the MVA region from 0 to 0.5. This result is not the same as others that the true K_L^0s have the peaks close to 1. Therefore, the training sample which is K_L^0 enhanced or not influences the training much more than using the different value of parameters.

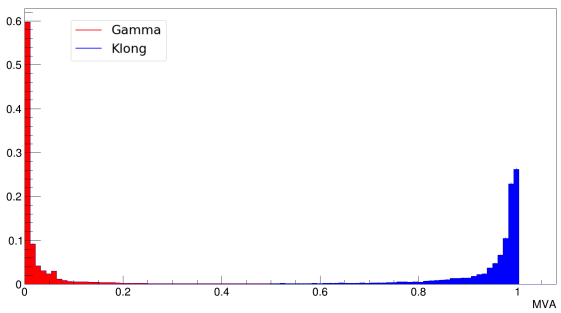

(a) nTrees:1000, nLevels:3

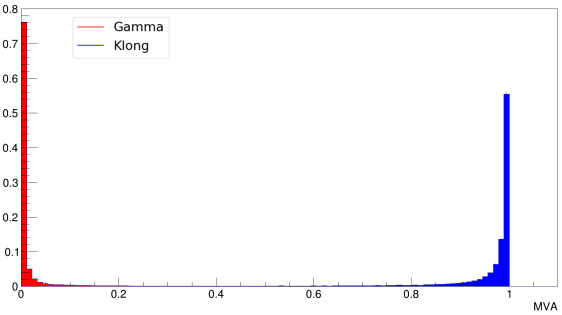

(b) nTrees:1000, nLevels:6

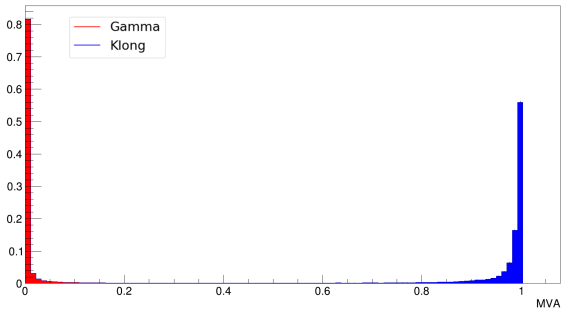

(c) nTrees:1000, nLevels:8

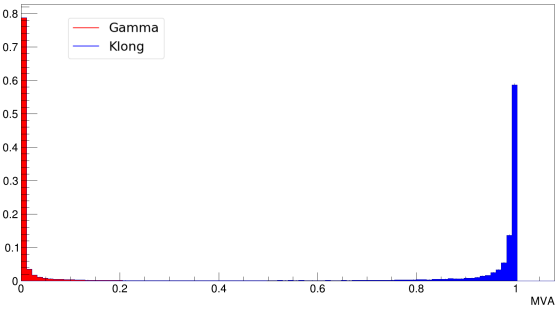

(d) nTrees:10000, nLevels:3

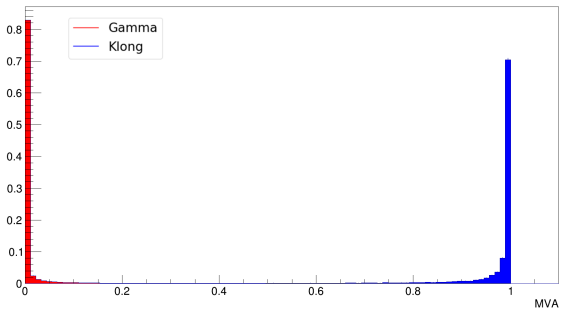

(e) nTrees:30000, nLevels:3

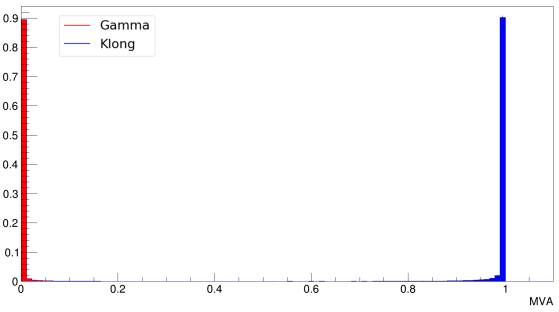

(f) nTrees:10000, nLevels:8

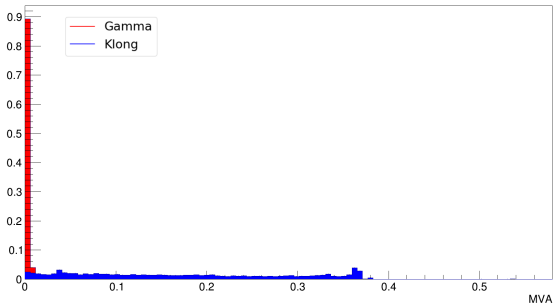

(g) nTrees:1000, nLevels:3 (Training sample without K_L^0 enhanced)

Figure A.1: The MVA distribution of the different training results.